Additive Manufacturing 127 (2026) 105303

Contents lists available at ScienceDirect

Additive Manufacturing

journal homepage: www.elsevier.com/locate/addma

Research paper

Captured: High-fidelity measurements of spatter sizes, shapes, and landing sites within a laser powder bed fusion machine

Nicholas O'Brien [a], Jordan Weaver [b,*], Satbir Singh [a], Jack Beuth [a]

[a] Department of Mechanical Engineering, Carnegie Mellon University, 5000 Forbes Avenue, Pittsburgh, 15213, PA, USA
[b] National Institute of Standards and Technology, Engineering Laboratory, Gaithersburg, MD, USA

ARTICLE INFO

Dataset link: data.nist.gov, https://doi.org/10.18434/mds2-4277

Keywords:
Spatter contamination
Laser powder bed fusion
In-situ monitoring
EOS M290
Spatter transport

ABSTRACT

Parts produced by laser powder bed fusion of metals (PBF-LB/M) continue to suffer from defects caused by spatter particles, byproducts of the melt-pool and vapor plume, that land on parts during printing and limit broader adoption of the process. Prior studies have detected spatter landing sites using in situ imaging, but these techniques often miss particles and provide imprecise size measurements. To compensate, ex-situ imaging is commonly used to measure spatter sizes and morphologies; however, the methods used to collect spatter samples often obscure the correlation between a particle's size or morphology and its landing location. This correlation is essential for understanding spatter induced defects and for validating spatter transport models. This manuscript presents results from an experiment designed to observe this correlation with higher fidelity than in previous work. Spatter particles from a single printed layer were captured using a tacky sheet metal plate that covered the build area, preserving particles at their original landing locations. This approach enabled high resolution measurements of landing positions, particle sizes, and morphologies. The general nature of the size distribution and appearance of agglomerates for the single experiment agrees with other studies on different machines, parameters, and alloys. The new capture method then revealed new insights: particles larger than 100 µm tend to be nonspherical agglomerates, which may help explain why the largest particles—surpassing 200 µm—can travel up to 150 mm downstream from the part. The high-fidelity measurements of size and landing sites are further discussed from the context of process monitoring, where it may be possible to detect only the largest spatter particles as a proxy for smaller ones.

1. Introduction and background

Laser powder bed fusion of metals (PBF-LB/M) is an additive manufacturing (AM) process that is being used in the aerospace, defense, and medical industries [1], but the process still often fails to produce defect-free parts. Some of these defects are caused by spatter particles, which are particles ejected as a byproduct of the printing process, depicted in Fig. 1. Spatter particles are of concern because of their correlation with porosity, found by several prior works [2–6].

The exact mechanism through which spatter particles cause porosity is still unknown. The theory with the most evidence is that particles larger than the virgin powder are too massive to melt completely, causing Lack-of-Fusion (LOF) pores when immediately interacting with the melt-pool [3,5–8]. This theory is supported by the experiments that have found partially melted, large particles on the walls of LOF pores [3,5,9], and a positive correlation of spatter size to pore size from Snow et al. [10]. Additionally, these larger particles can weld themselves to the part surfaces, increasing surface roughness [2,4,11–16]. Both porosity and surface roughness can act as crack initiation sites, leading to reduced high-cycle fatigue performance [2,12,17,18]. Secondarily, spatter is known to develop oxides on particles that will remain after a post-build sieve [2,4,13,19,20], which can increase oxygen in the powder and reduce a part's ductility [21]. In newer multi-laser systems as well, the hazards of spatter are shown to become more prevalent [22]. For these reasons, many prior works have developed in-situ process monitoring techniques for detecting the landing locations of spatter particles to track and mitigate the issues they cause.

Some spatter particles differ from the original powder in size, color, and/or temperature, each of which can be used to detect their landing locations when landing on the original powder. Visible light optical

* Corresponding author.
E-mail address: jordan.weaver@nist.gov (J. Weaver).

https://doi.org/10.1016/j.addma.2026.105303
Received 10 April 2026; Received in revised form 15 June 2026; Accepted 16 July 2026
Available online 24 July 2026
2214-8604/Published by Elsevier B.V.

cameras can observe spatter particles due to their darker color against the powder bed [23–26]. Infrared (IR) and near-IR cameras can detect the radiation emitted by particles, working best with "hot" spatter particles[1] [5,6,27,28]. Finally, spatter particles can be identified by their size/height difference using coherence scanning interferometry, fringe projection, or laser profilometry, as shown in Ikeshoji et al. [29], Brummerloh et al. [30], and Berez & Saldaña [26], respectively. These imaging methods produce height maps of the build area with a high resolution along the powder bed's height, through which spatter particles can be identified. However, some spatter is also powder that has simply been picked up and moved by gas entrainment without a clear change in physical condition [31], which would make these particles harder to detect with any of the aforementioned methods.

In-situ monitoring techniques are suitable for identifying spatter particle landing locations, but their resolution on the powder bed is too large to measure size or morphology. For example, Uddin showed in his doctoral thesis that an IR camera could detect the landing locations of spatter particles on the powder bed, but the apparent sizes of these particles ranged from 200 µm to 2,000 µm [27]. These measurements were likely biased because spatter particles larger than 400 µm have not been reported in literature. The other spatter detection methods discussed also have a coarse resolution along the build area, limiting their potential for measuring the sizes of spatter particles directly. Thus, it is often required to measure sizes and morphologies of spatter particles through more precise ex-situ analyses.

For ex-situ analysis, spatter particles must be removed from the machine to be observed in another measurement tool. There is no standardized method for acquiring a sample of spatter from the machine, but prior works have shown the following methods: gathering on carbon-tape after the build [13,26], retaining sieve waste [7,24,32], capturing powder and spatter in bins printed alongside other parts [6], or capturing spatter on mechanized plates above the powder bed after each layer [33]. The captured particles' sizes can generally be analyzed through several methods, such as optical microscopy, scanning electron microscopy (SEM), or laser diffraction [6,7,13,24,34]. SEM also allows for simultaneous observation of the chemical composition of oxides on spatter particles [5,13,20]. The reader is directed to Slotwinski et al. [34] for an overview of various other ex-situ analyses for characterizing powder/spatter.

While ex-situ techniques provide precise measurements of spatter, the prior methods of sampling spatter from a PBF-LB/M machine have not captured the correlation between the landing sites of spatter particles and their sizes and morphologies. To date, prior works have used the aforementioned in-situ monitoring techniques to detect the landing sites of particles without the ability to determine a particle's size or shape. This correlation is important for validating spatter transport models (see Refs. [28,35,36] for examples of these models) and for understanding which types of spatter particles correlate to defects during printing. For example, if larger spatter particles are of the most concern when monitoring spatter contamination during the process, then it should be demonstrated that these types of particles can be detected reliably.

The current work demonstrates a potential solution to this problem through a new method to capture spatter particles — a sticky plate — which preserves the landing locations of particles during ex-situ analysis. The plate can be imaged by an optical microscope without disturbing the captured spatter, allowing simultaneous measurements of all spatter particles' landing sites, sizes, and morphologies. With landing locations preserved, this method allows for more focused investigations than prior works regarding how a spatter particle's size

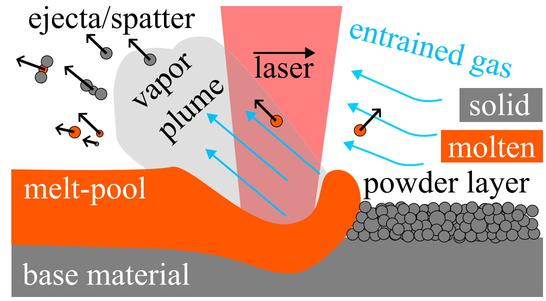

Fig. 1. Diagram of spatter generation at the melt-pool scale.

and morphology contribute to its landing location in the machine. The details of the capture plate and the experiment using it are discussed in Section 2, and the analysis of the recovered spatter particles is discussed in Section 3.

2. Methods

Section 2.1 discusses the printing conditions. Section 2.2 discusses how the spatter particles were captured with a metal plate, which we term a "spatter capture plate (SCP)", during the printing process. Section 2.3 discusses how images of the spatter capture plates were processed using a convolutional neural network (CNN) to identify spatter in images of the plates. Section 2.4 discusses the algorithm used to measure the spatter identified by the CNN. Section 2.5 introduces the metrics used to judge the CNN's performance, and Section 2.6 finally discusses the testing error of the CNN and how these errors affect the size/morphology measurements of spatter.

2.1. Printing setup

Experiments investigating defects caused by spatter, like the one presented in Snow et al. [6], often print a "spatter generator" that contaminates other parts with spatter to generate defects. Similarly, computational works like that from Anwar et al. [32] will print a single part and analyze the resulting spatter particles' landing sites for validation of a spatter transport model. The design of the following experiment is inspired by these practices.

Fig. 2a shows details of the printing process. A rectangular coupon measuring 25 mm by 10 mm was printed in an EOS M290 PBF-LB/M machine[2] from virgin nickel superalloy 625 powder.[3] The location of this part is roughly 100 mm downstream from the machine's lower nozzle, which is the point at which the inert gas flow attaches to the build plate in this machine [28,37]. The inert gas atmosphere was argon with a gas flow setting of 56 Pa (0.56 mbar), which corresponds to an average velocity of about 5.4 m/s in the tubing behind the machine, according to O'Brien et al. [28].

To establish steady-state process conditions, the part was printed for 125 layers with nominal parameters: laser power and speed of 285 W and 960 mm/s, respectively. Then for the layer at which spatter was captured, keyholing parameters were used, following the design of the spatter generators from Snow et al. [6]: a laser power and speed of

[1] An optical camera can be converted to a near-IR camera with an optical bandpass filter, allowing only a specific range of non-visible wavelengths to the sensor. However, this can drastically reduce the amount of light reaching the sensor, necessitating the use of longer exposure times to achieve a usable image, as noted in Schwerz et al. and Snow et al. [5,6].

[2] Certain commercial equipment, instruments, or materials are identified in this paper in order to specify the experimental procedure adequately. Such identification is not intended to imply recommendation or endorsement by NIST, nor is it intended to imply that the materials or equipment identified are necessarily the best available for the purpose.

[3] Dynamic image analysis (DIA) was used to measure the particle size distribution of the virgin powder. Powder was grab sampled from one 10 kg container and was used for three measurement runs. Averages and standard deviations are reported.

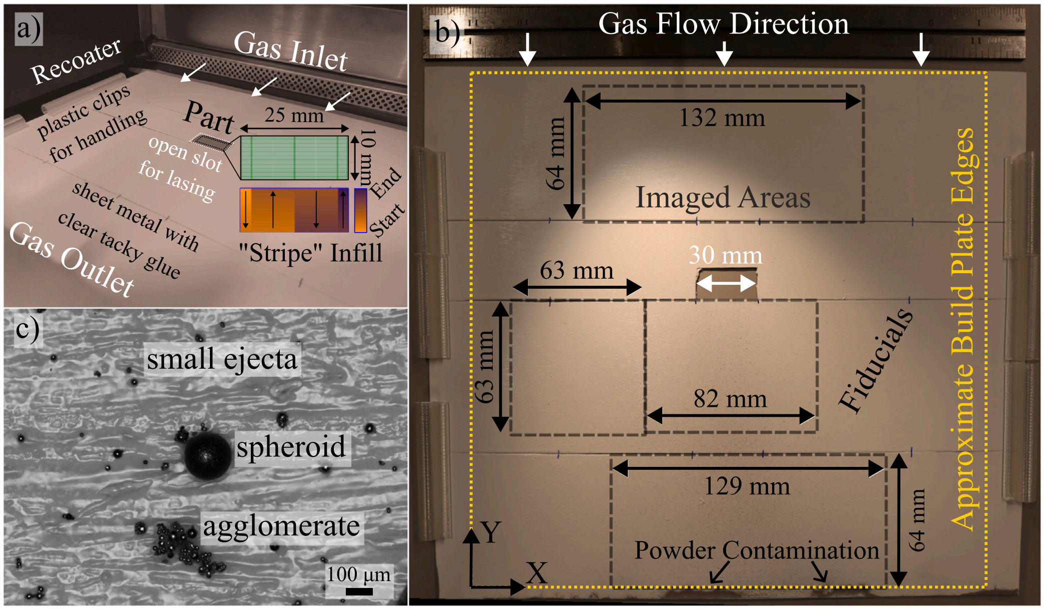

Fig. 2. Experiment setup. (a) Photo of spatter capture plate (SCP) in the PBF-LB/M machine build chamber, (b) Photo of SCP after printing, annotated with areas imaged via ex-situ optical microscopy, (c) Example z-stack image from the optical microscope.

300 W and 250 mm/s, respectively. The part was printed with a nominal layer height of 40 μm and a hatch spacing of 0.11 mm. The PBF-LB/M machine's laser has a D86[4] diameter of 72 μm [38]. The scan strategy for the layer of interest was a stripe pattern, as shown in the inset of Fig. 2a.

2.2. Recovering spatter with spatter capture plate

Spatter particles from the last layer of printing were captured with a spatter capture plate (SCP). The SCP is a 0.40 mm-thick sheet of metal with a matte white color and a tacky coating (Aleene's Original Tack-It Over&Over[5]) to hold captured spatter near their original landing locations. This behavior is confirmed by high-speed imaging of powder landing on a test SCP in Appendix D.

The SCP was constructed from four smaller plates due to size limitations of the optical microscope used in later steps. Fiducial marks were made to identify the relative position of each plate during the imaging step. The seams between these plates were sealed with tape to prevent accidental powder contamination during placement. One section of the SCP has a cutout for the scan area measuring 30 mm by 15 mm (2.5 mm larger than the part on all sides), which should allow enough room for normal powder denudation and spatter production [39].

Immediately after the last nominal layer was printed and the next layer of powder was spread, the SCP was placed on the powder bed such that the bottom edge of the plate was flush with the wall near the machine's outlet. During placement of the plate, some powder spilled onto the bottom edge of the plate. This contamination is visible at the very bottom of the SCP in Fig. 2b. The effects of this contamination will be discussed in Section 3. After placement, a steady inert gas flow and oxygen content below 0.1 % were re-established before printing the layer and capturing spatter.

[4] The D86 diameter of a gaussian beam is the diameter of a circle centered at the beam's centroid that contains 86 % of the beam's power.

[5] Early attempts at this experiment used carbon tape for compatibility with scanning electron microscopy (SEM), but these tapes had microscopic circular features that made it more difficult to discern between a captured particle and the background. The glue used in the current work is not conductive, so future works could benefit from exploring other thermally/electrically conductive adhesives that enable more material characterization techniques.

After printing, the areas outlined in Fig. 2b (labeled "Imaged Areas") were imaged using a Zeiss Axio Imager.Z2m. An example image from the microscope is shown in Fig. 2c. The 10× objective was used, yielding a pixel resolution of 0.3485 μm/pixel. The areas shown in Fig. 2b were imaged as a series of composite z-stack images, forming a sharp image of the subject along its height. The z-stack images were taken from 0 μm to 200 μm above the plate's surface at 8 μm intervals. Thousands of these z-stack images were taken across the plate and were stitched together, forming a single grayscale TIFF file around the size of 100 GB. Each imaged area took about two days to image. The imaging settings were selected to balance the tradeoff between image resolution/quality, file size, and time to image a region.

2.3. Identifying spatter using machine learning semantic segmentation

The images of the SCP were then processed to identify and measure the spatter that landed on them. Initial attempts with traditional computer vision approaches did not yield favorable results (detailed more in Appendix A), so a machine learning approach was chosen for this task. As visible in Fig. 2c, the glue has a textured background and the particles often have white dots from the reflection of the microscope's light. These different features can be learned by a machine learning segmentation model to identify whether pixels belong to the background or a spatter particle.

The training dataset for this machine learning model was formed as a subset of the imaged regions in Fig. 2b. Each of the imaged areas from the microscope were split into tiles measuring 2,048 pixels by 2,048 pixels, resulting in 51,784 tiles, total. A sample of 447 of these tiles formed the training dataset, 420 of which were randomly sampled from the images (stratified to be 105 per imaged area in Fig. 2b) and 27 of which were hand-picked containing images of the fiducial marks and other non-spatter objects. Due to the majority of random sampling, the training dataset represents a spatial distribution of the imaging conditions across the SCP. This training dataset was also split into five non-overlapping subsets for a 5-fold cross-validation analysis of the segmentation model, discussed in Section 2.6. All images were normalized to be between 0 and 1 according to the minimum and maximum value of the 16-bit images, 0 and 65,535, respectively.

Because of the difficulty in automatically identifying spatter particles with traditional computer vision techniques, each of the tiles

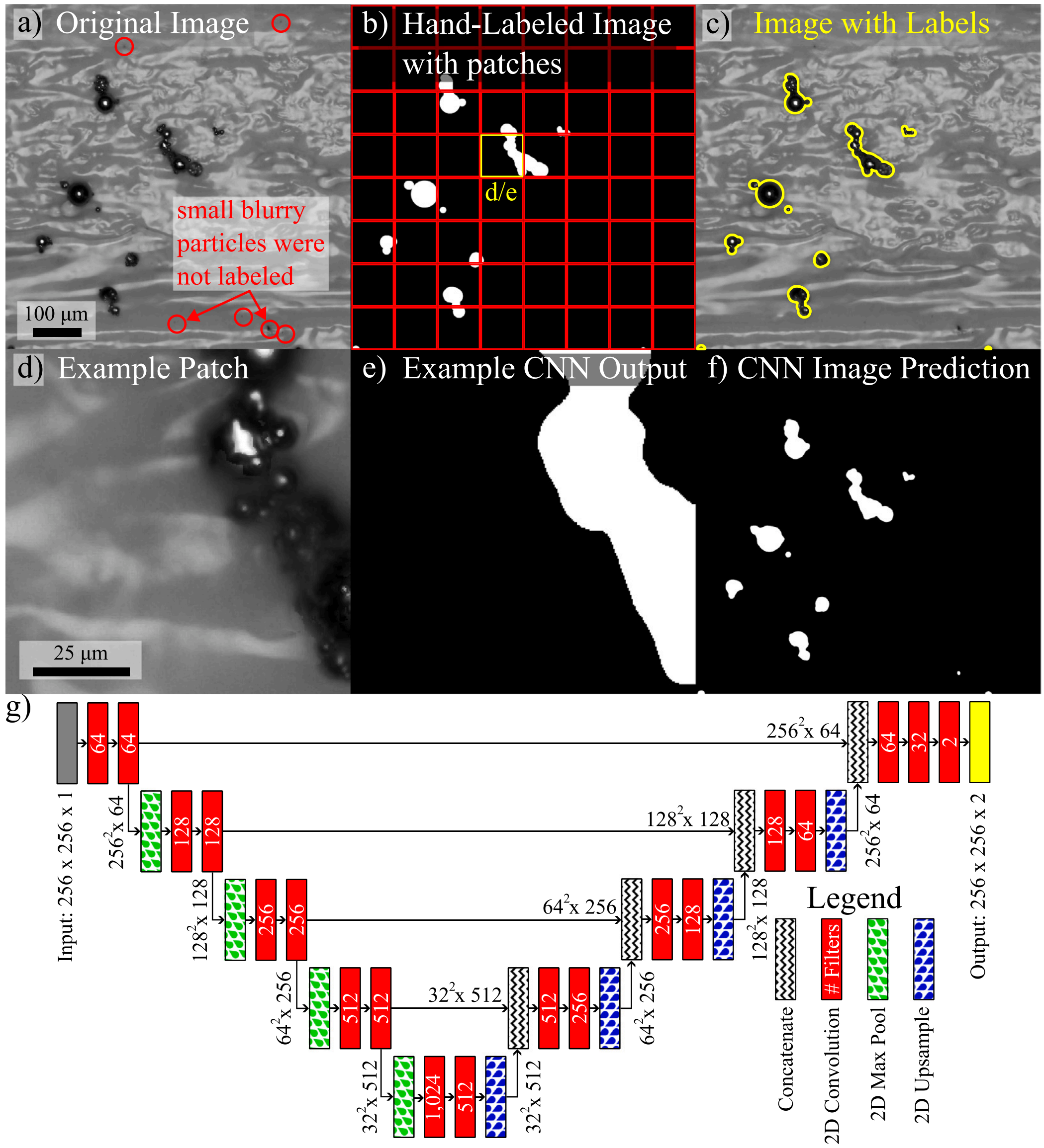

Fig. 3. Labeling data for the CNN and its architecture. (a) Example two-dimensional (2D) image of the SCP, (b) Hand-labeled image corresponding to a, on which the CNN is trained to replicate, (c) illustration depicting how the hand-labels correspond to the original image, (d) an example of a patch that would be provided to the CNN as input, (e) the output from the trained CNN for the patch in subfigure d, (f) the prediction returned by Dragonfly Workstation after compiling the predictions for each patch, and (g) U-Net architecture of the CNN for semantic segmentation. Subfigures a, b, c, and f share the scale-bar in a. Subfigures d and e share the scale-bar in d.

in the training dataset were hand-labeled, as shown in Fig. 3a–c. To remain consistent during labeling, all tiles were labeled by the same operator according to the following rules: (1) label all pixels belonging to a spatter particle and the surrounding background as spatter ("1"), up to 3 pixels away from the particle's edge, (2) label blurry areas for particles with a partially blurry section as spatter ("1"), and (3) label particles smaller than 10 pixels across as the background ("0"), for they may be soot or another contaminant—not spatter particles. There were also some fibers and other microscopic contaminants that likely came from the lab environment—these were labeled as the background, too. The borders in Fig. 3c show the accuracy of the hand labels, which closely follow the contours of spatter particles.

The machine learning segmentation model is a convolutional neural network (CNN) and has a U-Net architecture, similar to what is shown in Ronneberger et al. [40]. The U-Net architecture applies convolution, max-pooling, and up-sampling operations to each input image, as shown in Fig. 3g, to calculate a final segmented image mask. These operations allow the model to observe textures/features in the training dataset at different scales to identify what makes a "spatter pixel" differ from a "background pixel".

The program Dragonfly Workstation [41] is used to train and use the CNN. While the tiles are 2,048 pixels by 2,048 pixels, the tiles are first split into non-overlapping patches measuring 256 pixels by 256 pixels as input to the model, resulting in 64 patches per tile (see Fig. 3b–e). Patching is done due to memory limitations of the Graphics-Processing Unit (GPU) during both training and inference, and the output of the network is automatically reassembled to the original tile size by Dragonfly Workstation [41]. The pixels at the edge of patches are reflected to avoid edge artifacts in the predicted segmentation. The lack of artifacts at patch edges can be seen in Fig. 3f, which shows an example patch-reconstructed CNN prediction.

The model was trained with the categorical cross-entropy loss using the AdaDelta optimizer [42]. The batch size was set to 32 samples per epoch and the learning rate was started at a value of 1. Before starting training, a random sample of 20 % of the tiles (89 tiles) in the training dataset were withheld in a validation dataset. This validation dataset

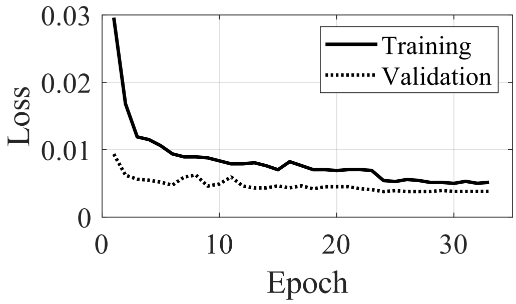

Fig. 4. Training and validation loss of CNN during training.

was used to determine learning rate reduction and early stopping, both of which help prevent overfitting. First, the learning rate was reduced by a factor of 0.1 if the loss on the validation set did not decrease after five epochs. Training would then be stopped early if the validation loss did not decrease more than 0.0001 after ten epochs, including the five epoch delay before reducing learning rate. At the end of training, the epoch with the best-scoring validation loss was retained as the "final model".

Training of the final model took 33 epochs because the validation loss did not decrease by more than 0.0001 within the last ten epochs, as shown in Fig. 4. The training loss does not decrease smoothly in Fig. 4 because the training dataset was augmented for each epoch to assist generalizability. With these random augmentations, the model was effectively trained on a slightly different training dataset every epoch, so the average training loss was not guaranteed to decrease after every epoch. The validation dataset, however, was not augmented each epoch, so its loss only decreases due to the improved performance of the model on unseen data. Further details regarding the CNN architecture and specific dataset augmentations can be found in Appendix B.

Finally, please note that this model was used to detect spatter particles across all images taken of the spatter capture plate. The performance of this model is evaluated via a 5-Fold Cross-Validation analysis, which is discussed in Section 2.6.

2.4. Measurement of spatter particles after segmentation

After training the CNN, the imaged regions were segmented by the CNN. Each segmented image consisted of 0's and 1's, representing background and spatter pixels, respectively. The segmented images were then passed through a custom `python` script to recognize contiguous groups of individual spatter pixels as spatter particles. This operation is more generally known as connected-components analysis in computer vision; an algorithm from the `opencv` [43] package was used for this step.

Once identified in a microscope image, the following characteristics of the identified spatter particles were measured: centroid X- and Y-position, minimum feret diameter, area, and perimeter. Fig. 5 shows how these quantities were measured for each spatter particle. First, any internal holes were filled. Then, the outer and inner contours were recovered using the `opencv` function `findContours()`. The inner contour tended to underestimate spatter particle measurements, yet the outer contour tended to overestimate them, so both contours are measured and averaged for every particle. Area and perimeter of each contour are measured using the `opencv` functions `contourArea()` and `arcLength()`, respectively. The minimum feret (also known as the "caliper measurement") is calculated through a custom function that first finds the convex hull of the contour and then calculates the minimum width of that hull.

Circularity, C, is reported in the current work to describe the aspect ratio of a spatter particle. Circularity is derived from the measured area, A, and perimeter, P, for each particle:

$$C = \frac{\sqrt{4\pi A}}{P} \tag{1}$$

For a perfectly circular particle, the circularity will be 1.0 and less than 1 otherwise. Circularity is used here as a 2D analogue for particle sphericity, Φ, which is also 1.0 when a particle is perfectly spherical and less than 1 otherwise.

Particle size distributions are generally weighted by a particle's volume, V, when reported in other works. The imaging method used in this work cannot measure the volume of a particle directly, so it must be derived from the particle's area as follows:

$$V = \frac{\pi}{6} D_{eq}^3 \text{ where } D_{eq} = \sqrt{\frac{4}{\pi} A} \tag{2}$$

Note that this volume-weighting method is only used when comparing directly to experimental works. Otherwise, all particle size distributions and derived quantities (e.g., the 10th, 50th, and 90th percentiles of particle size) are weighted by a spatter particle's measured area.

All measurements were converted from pixels to micrometers using the pixel size for the microscope's 10X objective: 0.3485 μm/pixel. The centroid positions of the particles in each image were transformed to the PBF-LB/M machine's reference frame using the known coordinates of the part on the build area and the fiducial marks on the spatter capture plate. The origin of the PBF-LB/M machine's coordinate system is shown in Fig. 2b at the lower left-hand corner of the build plate. Finally, if a detected spatter had a minimum feret less than 3 μm (approximately 10 pixels), then it was excluded from analysis because these particles usually did not belong to a spatter particle, and they are likely not related to spatter-induced lack-of-fusion defects, according to current theorized defect-formation mechanisms [7].

2.5. Definitions of segmentation model performance metrics

The segmentation model directly predicts whether a pixel in the provided image is a spatter pixel or a background pixel. To first judge the raw pixel-wise performance of the segmentation model, precision and recall are used, which can be calculated using the following:

$$\text{Pixel Precision} = \frac{\text{Correct Spatter Pixels}}{\text{\# of Spatter Pixels Predicted}} \times 100\ \% \tag{3}$$

$$\text{Pixel Recall} = \frac{\text{Correct Spatter Pixels}}{\text{\# of Spatter Pixels in Labels}} \times 100\ \% \tag{4}$$

Both precision and recall vary from 0 % to 100 %, with 100 % being a perfect assessment. Precision measures how many of the segmentation model's predictions are correctly spatter pixels (i.e., given the prediction is a spatter pixel, how likely is it to be correct?), and recall measures how many of the labeled spatter pixels were correctly identified (i.e., given a pixel that is known to be spatter, how reliably will the model identify it?).

The measurements presented in this work are based on individual particles, which are contiguous groups of pixels classified as spatter, as discussed in Section 2.4 and shown in Fig. 5. To capture the performance of the segmentation model on the positions, diameters, and circularities of spatter particles, "particle-wise" metrics are necessary. Towards particle-wise metrics, the particles identified in the label and the prediction must first be matched.

Two particles are considered a match if (1) the two particles' centroids are closer to one another than any other possible match, (2) the particle from the prediction lies within two radii of the label's particle, and (3) the segmentation model's particle is larger than 3 μm. Occasionally, there are multiple particles from the prediction that could be a match to a particle in the labeled image; in those cases, only the closest particle is considered a match and the remaining particles are considered unmatched (they would be false positives). After matching, particle-wise precision and recall can be calculated:

$$\text{Particle Precision} = \frac{\text{Correctly Matched Particles}}{\text{\# of Predicted } \textbf{Particles}} \times 100\ \% \tag{5}$$

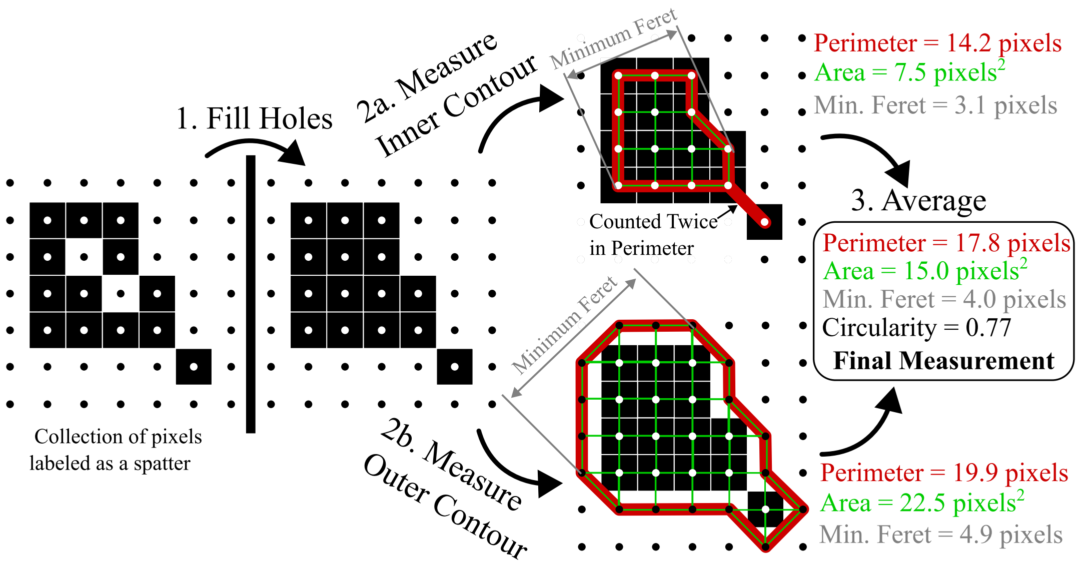

Fig. 5. Depiction of how spatter particles identified by the CNN and connected components analysis are measured.

$$\text{Particle Recall} = \frac{\text{Correctly Matched Particles}}{\#\text{ of }\textbf{Particles}\text{ in Labels}} \times 100\ \% \tag{6}$$

The particle-wise precision and recall have similar meanings to their pixel-wise counterparts; particle-wise precision measures how often the segmentation model's predicted spatter particles are correct, and recall measures how often the model will correctly identify spatter particles in an image.

After matching particles between the labels and the predictions, it is also now possible to compare their diameters and circularities. The root-mean-square error (RMSE) is calculated for these measurements:

$$\epsilon_D = \sqrt{\sum (D_{pred} - D_{label})^2} \tag{7}$$

$$\epsilon_C = \sqrt{\sum (C_{pred} - C_{label})^2} \tag{8}$$

Due to the nature of the calculation, RMSE must exclude particles that had no match.

In practice, it will not be known which particles from the CNN are false predictions and which ones are true, which could introduce error into the reported distributions of particle diameter and circularity. To this end, the two-sample Kolmogorov–Smirnov (KS) test [44,45] is used to judge if the distribution of all particle diameters and circularities are significantly different from one another when using hand labels or when using the segmentation model. The KS test compares the two cumulative distribution functions (CDFs) and determines if the distributions are significantly different, given the number of samples in each distribution. The formal hypotheses of this test are:

H_0 : The two distributions come from the same underlying distribution

H_1 : The two distributions **do not** come from the same underlying distribution

The validity of the null hypothesis is judged with the KS statistic, $D_{n,m}$:

$$D_{n,m} = \max_x \left| F_{1,n}(x) - F_{2,m}(x) \right| \tag{9}$$

where n is the number of particles in the hand-labeled test dataset, m is the number of particles identified in the CNN-labeled test dataset, x is the measurement of interest (diameter or circularity), and $F_{1,n}(x)$ and $F_{2,m}(x)$ are the CDFs from the hand-labeled particles and CNN-predicted particles, respectively. Note that these CDFs include all particles from the CNN, accounting for their potential to disrupt the distribution. The null-hypothesis, H_0, is rejected if $D_{n,m}$ exceeds the following value:

$$D^*_{n,m} > \sqrt{-\frac{1}{2}\ln\left(\frac{\alpha}{2}\right)\left(\frac{1}{m} + \frac{1}{n}\right)} \tag{10}$$

where α is the confidence level, which is 5 % ($\alpha = 0.05$) in the current work. The KS test is performed for distributions of diameter and circularity separately, to determine if the CNN's predicted particles are significantly different in size or circularity across the dataset.

2.6. Estimate of performance of segmentation model through cross-validation

To predict the performance of the CNN on unseen data (i.e., to evaluate the tendency of the CNN to overfit to the training data), a 5-fold cross-validation analysis was performed. In this analysis, the training dataset is split into five non-overlapping subsets of 89 tiles, each. Four of these subsets are fused to form a new training set, on which the CNN is trained *from scratch*; the CNN is then tested on the remaining subset to gather performance metrics for that fold. This procedure is repeated a total of five times, so that each subset is used as testing data only once. The cross-validation analysis is more reliable than a single train-test split for estimating the model's performance on unseen data [46]. The results of this cross-validation analysis are reported in Table 1 and are discussed in the following text.

From Table 1, the CNN performs very well at identifying spatter particles in the imaged spatter capture plates. The range of particle-wise precision and recall for particles larger than 3 μm is between 89 % to 92 % and 96 % to 99 %, respectively. The exceptionally high recall indicates that when there is a spatter particle in the image, the CNN will detect a portion of that particle at least 96 % of the time, and in practice, the precision shows that at least 89 % of the particles predicted by the CNN will correspond to a real spatter particle (in other words, only 11 % of the particles will be extraneous). The particle-wise recall and precision improves for particles larger than 63 μm and 100 μm, where the CNN achieved metrics of 100 % in all folds except Fold 1, where its precision was 92 %.

The particles that are correctly identified by the CNN will also have a similar diameter and circularity. As shown in Table 1, the RMSE for diameter and circularity vary from 2.5 μm to 10.7 μm and from 0.05 to 0.07, respectively. These higher errors come from Fold 4 and Fold 1, the former of which is visually represented in the residual plots in Fig.

Table 1
Performance of segmentation model (CNN) on test data from cross-validation.

Metric	Size range	Fold 1	Fold 2	Fold 3	Fold 4	Fold 5
Pixel-wise precision (%)	N/A	92	93	93	**95**	**91**
Pixel-wise recall (%)	N/A	85	91	**92**	**82**	91
Particle-wise precision (%)	>3 µm	**96**	**99**	**99**	97	98
	>63 µm	**92**	**100**	**100**	**100**	**100**
	>100 µm[b]	**100**	**100**	N/A	**100**	N/A
Particle-wise recall (%)	>3 µm	90	**89**	**92**	90	90
	>63 µm	**100**	**100**	**100**	**100**	**100**
	>100 µm[b]	**100**	**100**	N/A	**100**	N/A
RMSE: Particle diameter[a] (µm)	>3 µm	7.3	4.0	**2.5**	**10.7**	4.9
RMSE: Particle circularity[a] (–)	>3 µm	**0.07**	**0.05**	0.06	**0.07**	0.06

[a] These metrics are only measured for particles that had a correct match to a particle in the label image.
[b] Some test folds contained no particles above this size, in which case the metric is listed as "N/A".

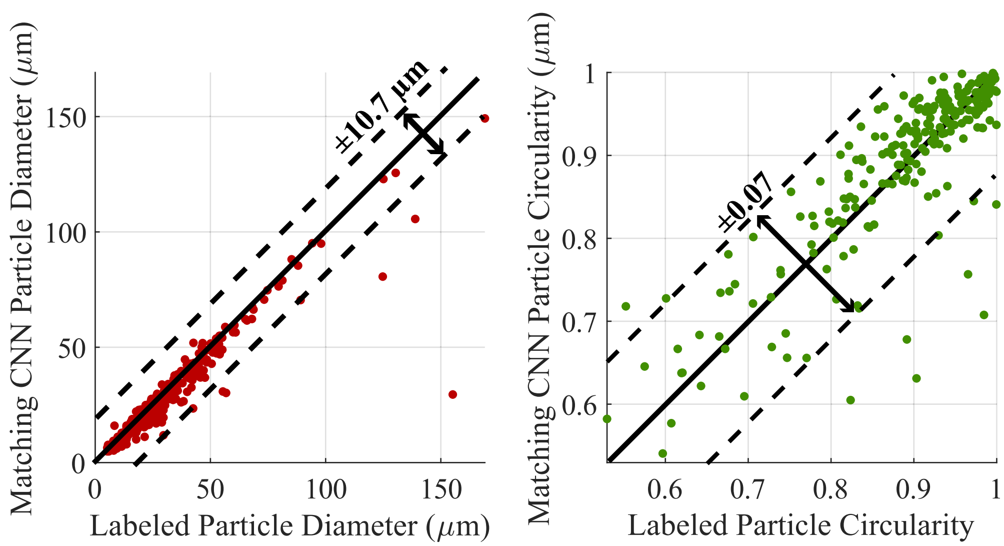

Fig. 6. Comparison of minimum feret diameter and circularity for spatter particles in testing dataset of Fold 4.

6. The errors in particle size and circularity are related to the pixel-wise recall, which measures the number of pixels in the labeled data that were predicted correctly. It is not surprising that the models with lower recall then have higher RMSE, like Fold 1 and Fold 4; these models seemed to struggle with identifying all the pixels in some spatter particles (seen by their pixel-wise recall), resulting in higher error for those particles' sizes and circularities.

The reduced recall in Fold 1 and Fold 4 can be attributed to the presence of large, partially blurred agglomerates that were present in those folds' testing data. These blurry agglomerates tend to look similar to the plate's background texture, causing less reliable segmentation of these types of particles, as discussed in Appendix C. However, these blurry particles are rare across the spatter capture plate (there were only five blurry particles across the 1,766 particles in the entire labeled dataset), so for most particles across the spatter capture plate, an RMSE of 10.7 µm for diameter and 0.07 for circularity can be considered a worst-case estimate for the CNN.

Finally, the **distribution** of the particles predicted by the CNN is not significantly different from the distribution of particles in the hand labeled images, according to the two-sample KS test. Fig. 7 shows an example of the test for the model trained in Fold 4. For this fold, the number of particles from the hand-labels and the CNN-predictions are $n = 400$ particles and $m = 430$ particles, respectively. Based on Eq. (10), the test fails if the difference between the two distributions exceeds 0.094 at any point along the graph, which is displayed by the shaded region in Fig. 7.

As seen in Fig. 7, both curves lie within the shaded region at all points for both diameter and circularity, meaning the KS test is passed and that the two distributions are not significantly different with a confidence level of 95 %. This test was passed for each cross-validation fold, meaning that the CNN used to process the remaining spatter capture plate data, which is trained on all the hand-labeled data, should also return size and circularity distributions that are not significantly different from the distributions if they had been labeled by hand. It should lastly be noted that the segmentation model is also only trained and tested on identifying spatter particles from nickel superalloy 625. Other alloys may appear with less contrast against the background of the SCP, altering the performance presented in this section. Future works that use different alloys may need to train their own model or at least fine-tune the model from this work to achieve similar segmentation results.

3. Results and discussion

The morphologies, sizes, and colors of captured spatter are discussed in Section 3.1. These results, where possible, are also contextualized with results from prior works to demonstrate the generalizability of the current work's results. Section 3.2 then shows how the spatter of different sizes are distributed across the build area and the implications for process monitoring techniques. Section 3.3 finally combines results from the first two sections by leveraging a nonspherical drag law to help inform current understanding of spatter transport in PBF-LB/M.

3.1. Morphologies and sizes of spatter

Fig. 8a shows a small sample of virgin powder as a reference. The virgin powder is generally metallic, reflective, and spherical with

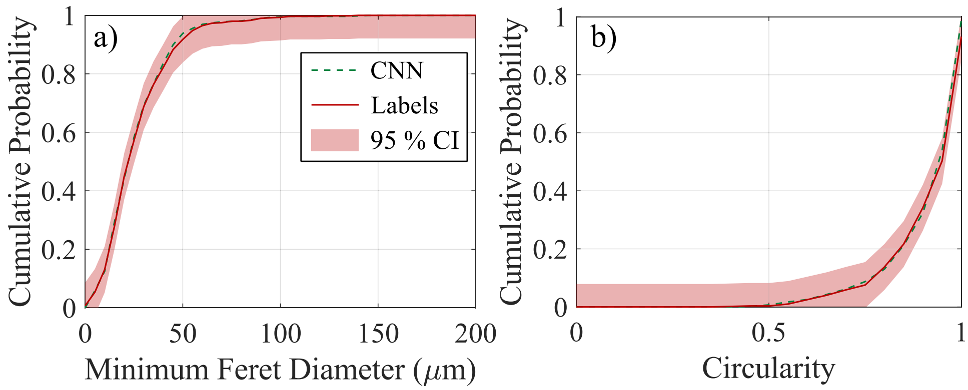

Fig. 7. Performance of segmentation model from Fold 4 on replicating the distribution of (a) minimum feret diameter and (b) circularity for its testing dataset. CI - Confidence Interval, calculated according to two-sample Kolmogorov–Smirnov (KS) test [44,45].

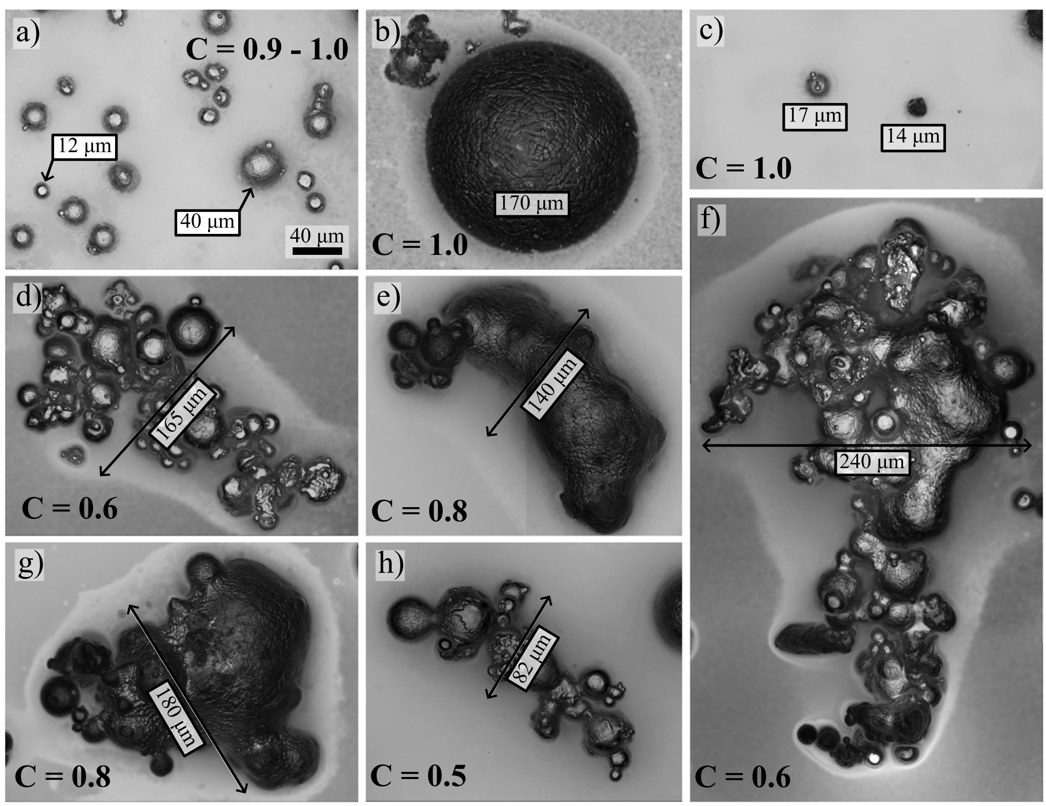

Fig. 8. Images of exemplary particles from the experiment, sharing the scale bar in subfigure a. (a) Sample of virgin powder (not from the spatter capture plate). (b) through (h) are spatter captured during the experiment. Note that these images were taken with the 50x objective (pixel resolution of 0.069 μm/pixel). These higher-resolution images were not used in the segmentation analysis. *C* is the circularity of the particle in that subfigure.

sizes smaller than 63 μm. There are some agglomerates and particles with smaller satellite particles. These satellite particles are common in powders produced by gas-atomization [34]. The captured spatter, shown in the other subfigures of Fig. 8, generally differ from the virgin powder through size, sphericity, and/or surface color.

First, the surface color of some spatter particles is darker than the original powder, represented well by the particles in Fig. 8b, c, e, g, and h. On the other hand, some spatter particles (Fig. 8d and f) are metallic with a surface quality similar to the virgin powder. The black surface texture on some spatter particles could be a marker of oxidation as shown in prior works [4,5,13,20]. This color difference can also be used to identify excessive spatter contamination as shown in Abranovic's thesis [23].

The sizes of spatter particles vary greatly and can be much larger than the original powder. This is first represented visually in Fig. 8c and f. Table 2 then shows how the D10, D50, and D90 (i.e., the 10th, 50th, and 90th percentiles of the minimum feret diameter, respectively) are consistently larger for the spatter distribution compared to the virgin powder distribution, with the largest spatter particle being around three times larger than the largest particle from the original powder.[6]

The wide range of spatter particle sizes has also been reported in several prior works [6,7,13,24,34], but only Gasper et al. [13] have reported the size distributions of pure spatter of all sizes.[7] Gasper

[6] While Section 2.6 found the CNN to reliably detect particles larger than 100 μm in the labeled data, each of the particles larger than 200 μm were manually verified due to their excessive size.

[7] Anwar & Pham [24] and Wang et al. [7] report the size distributions of spatter larger than 63 μm, making it difficult to compare fairly in Fig. 9. Snow

Table 2
Minimum feret diameter percentiles (Distributions plotted in Fig. 10a).

Units: μm	D10	D50	D90	Max
Virgin powder	19.4 ± 0.1	33.8 ± 0.2	51.4 ± 0.3	94.0
>3 μm, CNN	22.3	45.0	103	324

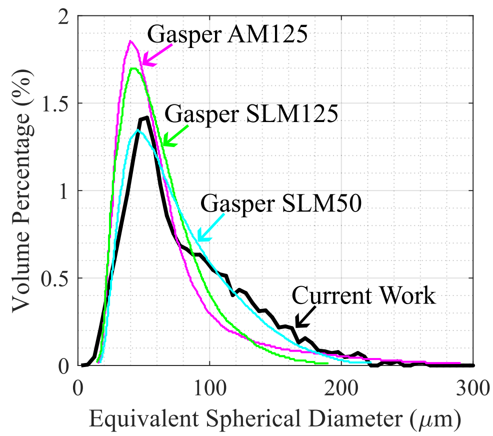

Fig. 9. Comparison of volume-weighted distributions of spatter particle diameters from current work and Gasper et al. [13]. AM125—Renishaw AM125 (*Renishaw plc, UK*); SLM125—SLM Solutions 125 (*SLM Solutions Group AG, Germany*); SLM50—ReaLizer SLM50 (*Realizer GmbH, Germany*).

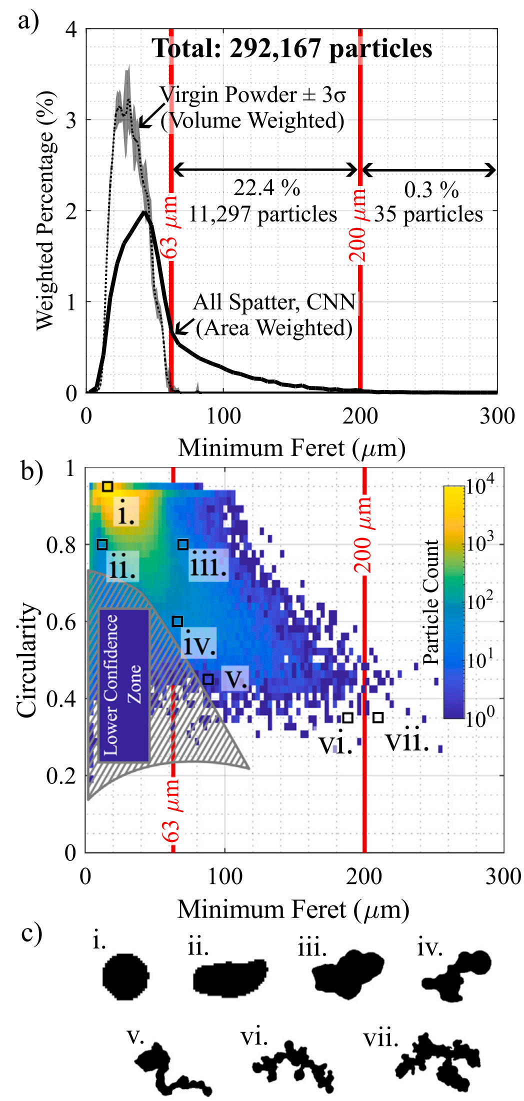

Fig. 10. Distributions of spatter sizes and circularities. (a) Minimum feret diameter, (b) 2D counts of circularity vs. minimum feret diameter (colorscale is logarithmic), and (c) Silhouettes of exemplary particles from b. Counts of “particles” refer to spatter found on the spatter capture plate.

et al. [13] recovered spatter produced from the printing of nickel superalloy 718 (an alloy in the same “family” as nickel superalloy 625) across three different PBF-LB/M machines with three different laser settings (pulsed vs. continuous, power, velocity, and beam size). The spatter were also gathered after printing several layers with powder from two different suppliers, making the results from Gasper et al. [13] more broadly applicable.

Despite having a much smaller scope (one layer on one machine) and using different laser settings, the size distribution from the current work fits within the variability shown by results from Gasper et al. [13], plotted in Fig. 9. Each size distribution from Gasper et al. [13] shows two similarities: the peak of spatter sizes sitting between 40 μm and 60 μm and long tails with very large spatter particles in excess of 200 μm. The current work's distribution holds this same shape. This agreement suggests that the spatter captured in the current experiment is likely a representative sample of all spatter particles. Thus, when analyzing the aspects of spatter not available in prior works with the new spatter capture method, it is predicted that this work will generalize to other materials and PBF-LB/M machines.

One of the measurements not reported in prior works is circularity, which aids in deducing the source of a spatter particle and how it will interact with the gas flow/vapor plume. When viewing Fig. 10a/b, most spatter particles are the same size and shape as the original powder. About 77.3 % of the spatter (as a fraction of total area of spatter) were in the size range of the original powder, being smaller than 63 μm. (Two example powder particles in this size range are shown in Fig. 8c.) Fig. 10b then shows that all of these smaller spatter particles were nearly circular, the same as the original powder.[8] It is likely that these circular, small spatter particles are a mixture of both (1) unaltered powder that was redistributed during printing and (2) altered (e.g., oxidized or melted) molten particles, but the exact proportions are unclear.

It can also be seen that larger spatter particles are generally non-circular, according to Fig. 10b–c. Fig. 8d–h then shows that these large, non-circular particles are agglomerates of smaller particles. These agglomerates are mainly formed from collisions between two or more liquid/solid spatter particles shortly after ejection, according to prior investigations [13,47,48]. In some cases, the laser can subsequently melt agglomerates mid-flight [48], which could explain the large spherical particle in Fig. 8b.

The large, non-spherical particles are not necessarily limited to nickel superalloy 625 or the laser settings used in this experiment. Prior investigations, like that of Young et al. [47], have reported agglomerate spatter particles across a wide range of process settings and for different materials like Ti6Al4V and AlSi10Mg, demonstrating the pervasiveness

et al. [6] and Slotwinski et al. [34] do report sizes across a similar range, but their results contain spatter and powder, which causes their distributions to be biased towards smaller sizes.

[8] The “Lower Confidence Zone” in Fig. 10b is a region that contained particles with circularities that did not correspond to actual particles in the original microscope images on the spatter capture plate. Some of these tiny non-circular particles were a result of blurry particles, which the CNN tends to “break up” into smaller, discontinuous blobs during segmentation. Appendix C discusses this phenomenon further.

of these particle types. Given that agglomerates tend to be large and that larger spatter particles are theorized to be a primary cause of the spatter-induced lack-of-fusion defects [2,4,5,7,8], the general nature of agglomerates is especially important to characterize.

3.2. Spatter landing locations and connection to sizes

The prior section showed that the distribution of spatter sizes was general across different machines and laser settings for comparable nickel superalloys (718 and 625). It also showed that the large agglomerate-type spatter particles are found across several alloys and laser parameters, further suggesting the generalizability of the spatter observed in the current work. While agglomerates were observed in high-speed videos, their landing locations, in particular, have not been observed in prior works.

This section will now present the landing locations of different sizes of spatter particles. These landing locations will be influenced by the particular gas flow in the EOS M290 PBF-LB/M machine, which is typically oriented towards the machine's outlet with a speed around 1 m/s. The reader is directed to prior measurements and simulations of the gas flow in this PBF-LB/M machine [28,37,49], which should make the following interpretations and observations more readily applicable.

First, most spatter lands downstream from the printed part, up to 150 mm away, as seen in Fig. 11a–c and e. To the left and right of the part, spatter particles are found in much lower concentrations, but they can still travel up to 100 mm in this direction. This finding is true for all sizes of spatter in Fig. 11: particles larger than 3 μm (11a), particles larger than 63 μm (11b), and particles larger than 200 μm (11c). The histogram of spatter travel distance in Fig. 11e (normalized by particle counts) also shows how more spatter particles land further from the part than near it.

This result is surprising for the largest spatter particles in Fig. 11b/c/e; intuition suggests that larger spatter particles would be ejected slower and would be less affected by the inert gas flow, causing them to land closer to the part [26]. Results in Fig. 11c/e contradict this intuition, showing that even the largest spatter particles can be transported over a large area of the build plate, potentially causing defects. It should be stated, however, that only 35 particles of this size were observed (see Fig. 10a), making the sample size very small in comparison to the other size ranges investigated.

With the similarity of the landing patterns and travel distances in Fig. 11, it may be sufficient for process monitoring tools to detect larger spatter particles as a proxy for all spatter particles. This similarity is seen best when comparing the landing densities of spatter larger than 3 μm (Fig. 11a) to the spatter larger than 63 μm (Fig. 11b). Both density maps have a high concentration of spatter immediately downstream from the part, with less spatter occurring to the left and top of the part. There is a large differences between these two plots near the bottom of the plate (near the gas outlet) and near the top of the plate (closer to the gas inlet), but these features should not be over emphasized. Since these acute features disappear for populations of spatter larger than 63 μm, it is likely that some of these particles came from the original powder when the plate was placed on the powder bed.

Because the two heatmaps measure the concentration of spatter with the same set of histogram bins, the spatial correlation between them can further be quantified through the linear correlation coefficient, r, calculated with the function `corrcoef` in Matlab [50]:

$$r = \frac{\mathrm{Cov}(X, Y)}{\sigma_X \sigma_Y} \tag{11}$$

where $\mathrm{Cov}(X, Y)$ is the covariance, σ is the standard deviation, and X and Y are the two variables being correlated. In this case, X is the set of densities measured from all bins in Fig. 11a, and Y is the set of densities measured from all bins in Fig. 11b.

Fig. 11d plots the concentrations of spatter for the two heatmaps versus one another, visualizing their correlation, which results in a linear best fit slope of 0.75 ± 0.01 (95 % confidence interval). This correlation is near 1, indicating a generally positive relationship between the two classes of particle size (larger than 3 μm and 63 μm). There is still significant variability not explained by the linear trend, though, suggesting that some information will be lost if only measuring the landing sites of particles larger than 63 μm.

With most process monitoring tools having projected pixel sizes near 70 μm (or larger), it is likely that these methods may only reliably detect spatter larger than 70 μm. If larger spatter particles could act as a proxy for judging the amount of smaller spatter particles landing in a region, then the hardware requirements for spatter monitoring could be relaxed. However, larger spatter particles are exceedingly rare, (there were only 11,332 particles larger than 63 μm out of 292,167 particles detected on the spatter capture plate), presenting fewer opportunities to detect egregious spatter contamination. With especially large 200 μm spatter particles only landing downstream from the part in this experiment, lower resolution process monitoring systems may also miss contamination in regions upstream from the part.

Finally, it is notable that the imaging conditions yielding the results in Fig. 11 were nearly pristine with a high-contrast background and consistent lighting. Some larger spatter particles can have a surface quality similar to the virgin powder (as discussed in Section 3.1), which will make them harder to differentiate from the background powder bed when using an optical process monitoring method. Similarly, some larger spatter particles may cool to near the temperature of the powder bed before landing, making these particles difficult to detect for infrared imaging methods. While the results in Fig. 11 could support the idea that process monitoring tools can focus on larger spatter particles without losing performance, this approach will come with additional challenges and considerations.

3.3. Agglomerates' landing locations and sphericities

Fig. 11b–c showed how spatter larger than 63 μm mostly landed downstream from the part. This trend could be a result of larger spatter particles' lower circularities/sphericities, which were presented in Section 3.1. This section will explore the impact of nonsphericity on a particle's drag, providing a potential mechanism to explain the travel distances seen in Fig. 11b–c.

First, nonspherical objects have a higher ratio of surface area to mass compared to a perfect sphere, meaning that they can be subjected to a higher drag force compared to a spherical particle of the same mass. Drag force, $\boldsymbol{F_D}$, is proportional to the drag coefficient, C_D, which is a function of the Reynolds number of the particle, Re_D:

$$\boldsymbol{F_D} \propto C_D(Re_D) \text{ where } Re_D = \frac{\rho_f \, |\boldsymbol{\Delta u}| \, D_p}{\mu_f} \tag{12}$$

where ρ_f is the fluid density (1.62 kg/m^3 for argon [51,52]), μ_f is the fluid molecular viscosity (2.13×10^{-5} kg/(m · s) for argon [51,52]), $\boldsymbol{\Delta u}$ is the difference between the particle's velocity and surrounding fluid's velocity, and D_p is the diameter of a sphere with the same mass as the nonspherical particle. Two particles with the same masses in the same flow conditions will have the same Reynolds number, regardless of their sphericities. Chen et al. [53] have performed direct numerical simulations of the flow around various random agglomerates; their drag correlation is presented here as an example, but this is still a field of ongoing research:

$$\begin{gathered} C_D = \frac{8}{Re_D}\sqrt{\frac{\Lambda}{\Phi_\perp}} + \frac{16}{Re_D}\frac{1}{\sqrt{\Phi}} + \frac{3}{\sqrt{Re_D}}\frac{1}{\Phi^{0.75}} + \frac{\Lambda}{\Phi_\perp}\left(0.42 \times 10^{D}\right) \\ \text{where } \Lambda = 0.035\Phi_\perp^{-4.9} - 0.44\exp\left(-0.43 Re_D\right) + 0.96 \\ D = 0.4\left(-\log_{10}(\Phi)\right)^{0.2} \\ \Phi = \pi D_p^2 / A_{surface} \\ \Phi_\perp = \frac{\pi}{4} D_p^2 / A_{projected} \end{gathered} \tag{13}$$

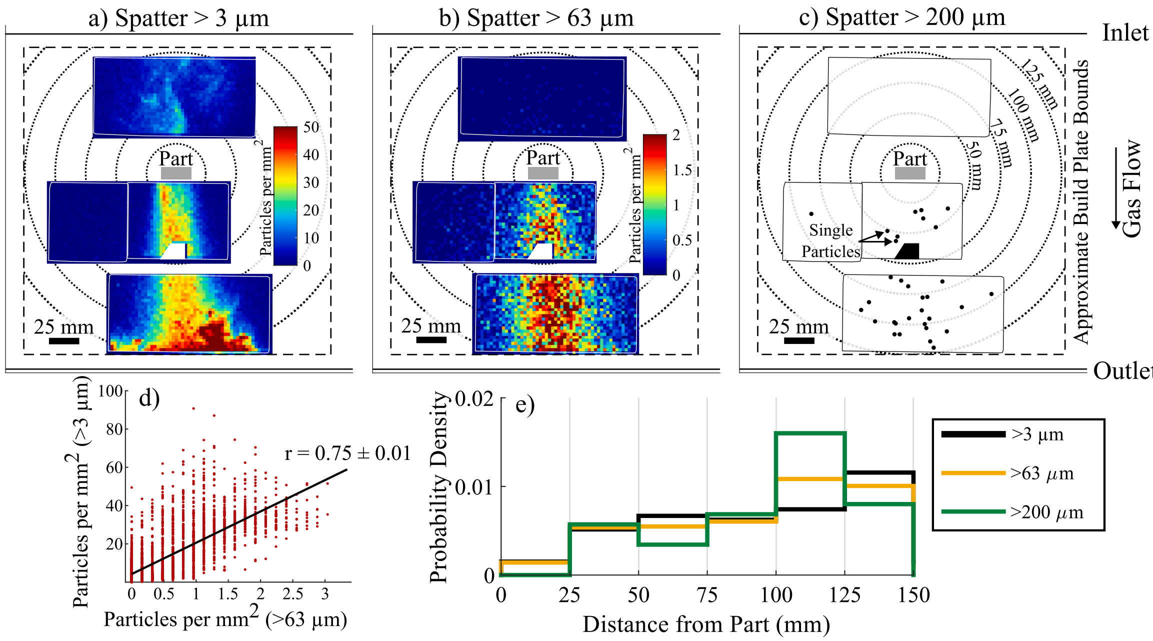

Fig. 11. Concentration of spatter particles from spatter capture plate. (a) concentrations for all spatter detected larger than 3 µm. (b) Concentration of spatter detected larger than 63 µm. (c) Scatter plot of spatter larger than 200 µm. (d) Scatterplot comparing the densities between bins in subfigures a and b. (e) Histograms of spatter particle travel distance from the part. Rings in subfigures a, b, and c indicate distance from the part centroid.

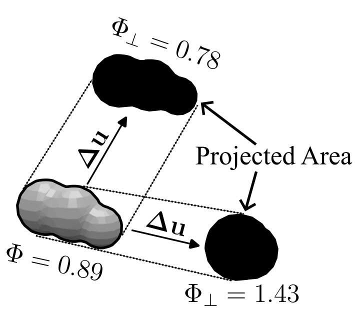

Fig. 12. Diagram showing how crosswise sphericity, $\Phi_\perp$, changes according to the particle's velocity/orientation relative to the surrounding fluid.

where Φ is the sphericity of the particle, $A_{surface}$ is the surface area of the particle, $\Phi_\perp$ is the crosswise sphericity, and $A_{projected}$ is the area of the particle's cross-section as viewed from the direction of the fluid flow relative to the particle. Crosswise sphericity is necessary to account for the particle's orientation, which is shown visually in Fig. 12.

While it is tempting to use the particle's circularity (Fig. 10b) in place of the true sphericity for computing the drag coefficient in Eq. (13), Rorato et al. [54] and Grace & Ebneyamini [55] both show that this should generally be avoided.[9] For this reason, the particles shown in Fig. 10c were modeled in a 3D modeling software with spheres of different sizes, forming an approximation of the original agglomerate, shown in Fig. 13a. These 3D models were then exported as `.stl` files and loaded into a custom `python` code, where their sphericities and crosswise sphericities were computed for 10,000 random orientations with the `trimesh` package.

Most orientations of particles yielded crosswise sphericities near their 3D sphericity, with fewer skewing towards values greater than unity, as seen in Fig. 13b. These distributions are only shown to demonstrate the trend and variation in crosswise sphericity for the modeled agglomerates. These distributions should not be taken as a general rule for agglomerates without further validation.

As a reference point for nonspherical particles, the spherical drag coefficient from Morsi & Alexander [59] is used[10]:

$$C_D = \frac{a_1(Re_D)}{Re_D} + \frac{a_2(Re_D)}{Re_D^2} + a_3(Re_D) \tag{14}$$

The coefficients a_1, a_2, and a_3 are reported in Morsi & Alexander [59], and they change according to the Reynolds number of the particle.

Fig. 14 shows how the drag on a nonspherical particle changes relative to drag on a spherical particle (the ratio of Eqs. (13) to (14)) for the three primary parameters of Eq. (13): sphericity, crosswise sphericity, and Reynolds number. Four Reynolds numbers are presented, representing particles of 50 µm and 200 µm in argon flows of 1 m/s and 10 m/s. The flow speed ($|\Delta \boldsymbol{u}|$) of 1 m/s represents particles interacting with the inert gas flow near the center of the EOS M290 build plate, which can be as high as 3 m/s in some areas [28,37]. The flow speed of 10 m/s represents particles interacting with the vapor plume (a phenomenon observed experimentally in Nassar et al. [48]). This speed is informed by simulations from Bidare et al. [61] and Ly et al. [31], but some prior works reported velocities as high as 100 m/s [62,63]. These velocities are thus subject to uncertainty and are only chosen to illustrate the expected range in Reynolds numbers of a spatter particle from ejection to landing.

[9] The shortcomings of 2D measurements of 3D particles has been well-documented in geological engineering fields. The reader is referred to Refs. [54,56–58] for an overview of some experimental techniques, such as micro X-ray Computed Tomography (μXCT) or other forms of multi-view imaging to measure one or more particles' sphericities.

[10] Barati et al. [60] show that Morsi & Alexander [59] is among the most accurate correlations for spherical particles.

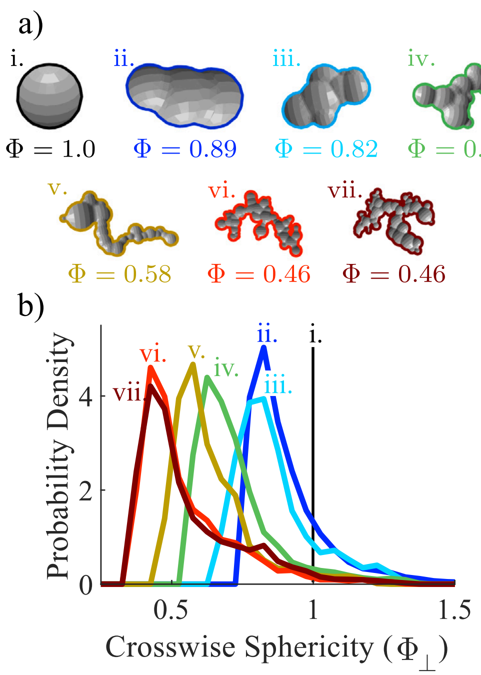

Fig. 13. (a) 3D models of particle silhouettes from Fig. 10c, listed with their calculated sphericity. (b) Distributions of crosswise sphericity after sampling across 10,000 random orientations for each particle.

Firstly, a nonspherical particle is generally expected to experience more drag than its mass-equivalent spherical counterpart. This result can be seen from the vertical lines labeled **i** through **vii** in Fig. 14, almost all of which sit in regions of greater than 1 (more drag than a sphere). Only two particles, **ii** and **iii**, have orientations where their drag would be lower than a sphere because those orientations present a *smaller* cross section to the flow than their spherical counterpart. This phenomenon has been reported in work of Hölzer & Sommerfeld [64], but even some of these smaller projected areas will experience more drag than a sphere at higher Reynolds numbers, as seen by particle **iii** at $Re_D = 152.1$.

This variation in crosswise sphericity has a drastic influence on the range of drag forces a particle will experience. In Fig. 14, the drag-ratio isocontours are nearly horizontal for crosswise sphericities below 0.5, showing the lack of sensitivity to the particle's 3D sphericity in this regime. Particles **vii** and **vi** have the smallest measured crosswise sphericities near 0.4, yielding an increase in drag by as low as 4 at the lowest Reynolds number ($Re_D = 3.8$) and as high as 10 at the highest one ($Re_D = 152.1$). It is currently unclear, though, whether particles have a preferred orientation during flight, and this analysis can only show the wide range of drag forces a particle could experience. It is also possible for particles to experience a Magnus force, a force due to their rate of rotation, which would add further complexity to a particle's flight [65], but the current investigation is not able to verify whether this phenomenon affects spatter particles.

These increases in drag force may help explain why the largest spatter particles, with shapes like particles **vii** and **vi**, were mainly found downstream from the part, even when intuition and prior research would suggest that larger particles would land closer to the spatter generating part. Non-spherical agglomerates would experience higher drag forces, whether interacting with the vapor plume ($|\boldsymbol{\Delta u}| = 10\,\mathrm{m/s}$) or the machine's inert gas flow ($|\boldsymbol{\Delta u}| = 1\,\mathrm{m/s}$).

First, Nassar et al. [48] have shown agglomerates to form through collisions near the part during printing, so an agglomerate could form in the vicinity of the vapor plume and be accelerated to a higher-than-expected initial velocity, resulting in a farther-than-expected travel distance [28]. Second, the increased drag on nonspherical particles could cause them to be carried further downstream by the machine's gas flow compared to if they were assumed spherical. In addition to this general increase in drag force, Fig. 14 shows there could be orientations of particles which will experience an order-of-magnitude higher drag force than a spherical particle under the right conditions, further adding to the potential reason for observing large agglomerates near the outlet of the machine. Prior computational works commonly make the assumption of spherical spatter when simulating spatter transport, but these results suggest that the assumption of spherical particles may introduce error when the spatter particles of interest are highly nonspherical.

4. Conclusions and recommendations

This work examined the spatter captured throughout printing a single layer of nickel superalloy 625 in the EOS M290 PBF-LB/M machine. Spatter particles were collected using a glue-coated sheet-metal capture plate that covered the entire build area, preserving particles at their original landing locations. This capture method enabled high-fidelity measurements of particle sizes, morphologies, and landing sites, which have not before been measured simultaneously to the same level of detail in prior works. The plates were imaged through optical microscopy, and a convolutional neural network was then used to identify spatter particles across the images for measurement. The ability to correlate particle size and morphology with precise landing locations is key for validating spatter transport models, refining in-process monitoring strategies, and determining which spatter particles are most strongly associated with defect formation.

Approximately 292,167 spatter particles were captured, 77 % of which (by total spatter area) were similar to the original powder: smaller than 63 µm and spherical. The remaining particles consisted of larger spheroids and nonspherical agglomerates, which prior research has identified as a primary contributor to spatter-induced lack-of-fusion defects. Importantly, the largest particles were more likely to be nonspherical because they were composed of multiple partially melted particles, consistent with the agglomeration mechanisms observed in earlier studies.

With the simultaneous measurement of spatter sizes and landing sites, this study is able to view the landing sites of specific sizes of spatter particles, which no prior work could do to the same level of detail. Most spatter landed directly downstream from the part, traveling up to 150 mm away. This trend held across particle sizes, including agglomerates exceeding 200 µm. Significantly fewer particles landed to the sides or upstream of the part. Because larger particles follow similar landing patterns to smaller ones, it may be possible for in situ monitoring systems to detect only the largest spatter particles as a proxy for the full spatter field, though this hypothesis requires further validation. Moreover, the imaging conditions in this experiment were nearly ideal, and practical attempts at this approach will likely encounter additional challenges.

Finally, spatter larger than 200 µm were found exclusively downstream from the part. This observation may be partially explained by the increased drag experienced by nonspherical particles; an agglomerate will experience a higher drag force than a spherical particle of equal mass under the same flow conditions. As a result, agglomerates may be ejected at higher velocities by the vapor plume and transported farther downstream by the gas flow. The common intuition that larger particles travel shorter distances than smaller ones should therefore be questioned in light of the present findings.

Despite the small scale of this experiment, many of the findings from this work are expected to generalize to other laser settings, machines, and materials based on prior works. Young et al. [47] also observed nonspherical agglomerates in Ti6Al4V and AlSi10Mg across a range of process conditions, and Gasper et al. [13] reported similar size distributions of spatter particles from nickel superalloy 718 across multiple

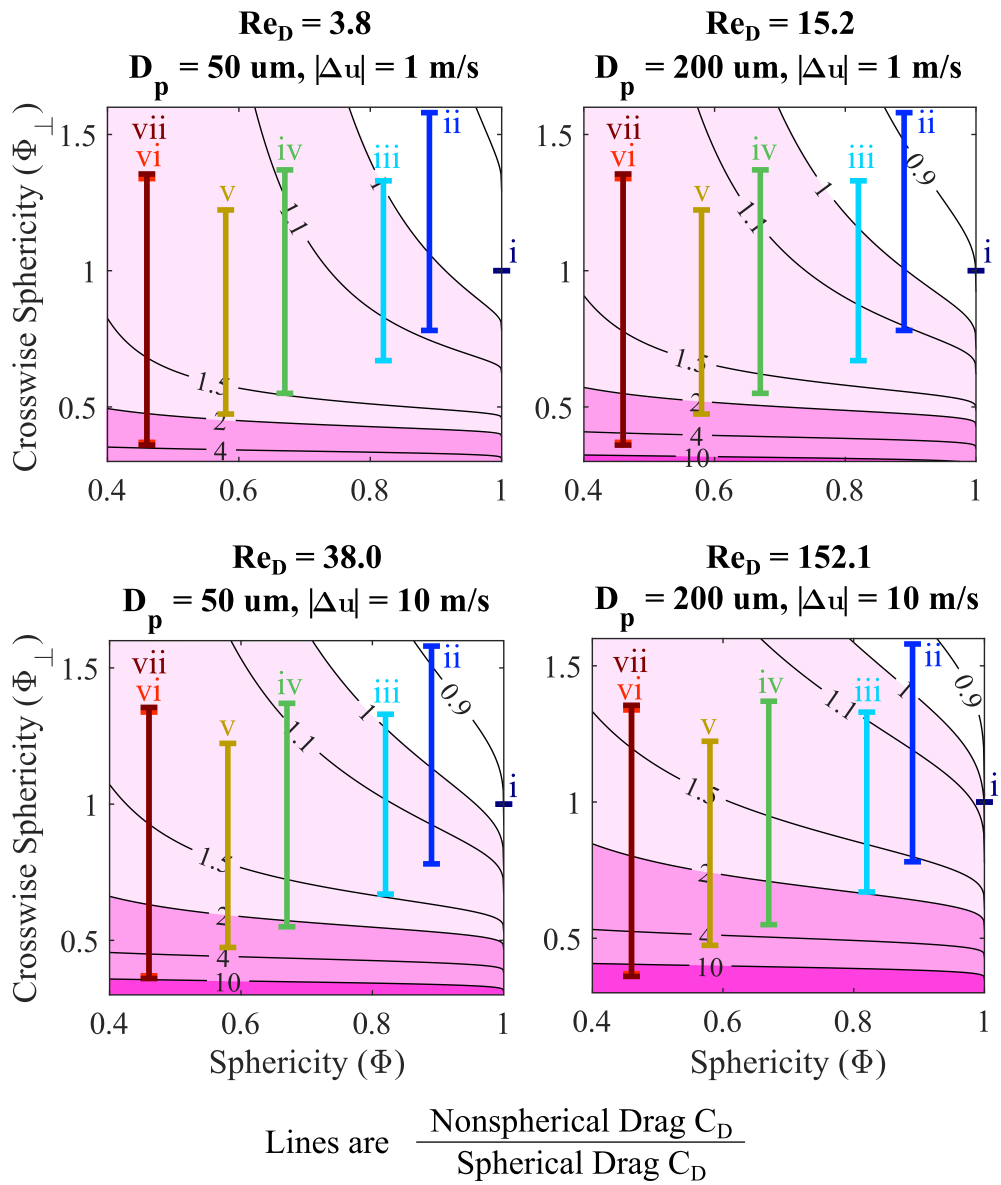

Fig. 14. Ratio of Eqs. (13) to (14) for different Reynolds numbers, sphericities, and crosswise sphericities. The ranges of crosswise sphericity for each particle from Fig. 13 are plotted as vertical lines to indicate the possible range of drag coefficients. Values of D_p and $|\boldsymbol{\Delta u}|$ are also listed for reference, with $|\boldsymbol{\Delta u}|$ being informed by the gas flow speeds of argon gas in PBF-LB due to the machine's cross flow [28,37] and the local high speeds entrained by the vapor plume [31,61].

machines and several layers. While the existence of agglomerates is well established, the present work is the first to track their landing sites across the full build area. Finally, the machine used in this study, the EOS M290, uses gas flow speeds that are typical when compared with other PBF-LB/M machines. Contextualized with prior studies, the relationships between particle size, sphericity, and landing locations are expected to appear in other materials and process conditions, but more experiments would be necessary to solidify this claim.

CRediT authorship contribution statement

Nicholas O'Brien: Writing – review & editing, Writing – original draft, Software, Methodology, Investigation, Conceptualization. **Jordan Weaver:** Writing – review & editing, Supervision, Resources, Methodology, Conceptualization. **Satbir Singh:** Writing – review & editing, Supervision, Conceptualization. **Jack Beuth:** Writing – review & editing, Supervision, Funding acquisition, Conceptualization.

Declaration of competing interest

The authors declare the following financial interests/personal relationships which may be considered as potential competing interests: Nicholas OBrien reports financial support was provided by US Army Research Laboratory. If there are other authors, they declare that they have no known competing financial interests or personal relationships that could have appeared to influence the work reported in this paper.

Acknowledgments

A portion of the research was sponsored by the Army Research Laboratory and was accomplished under Cooperative Agreement Number W911NF-20-2-0175. The views and conclusions contained in this document are those of the authors and should not be interpreted as representing the official policies, either expressed or implied, of the Army Research Laboratory or the U.S. Government. The U.S. Government is authorized to reproduce and distribute reprints for Government purposes notwithstanding any copyright notation herein. The authors would also like to acknowledge the NIST Fabrication Technology Office and Mr. Jared Tarr for help with fabricating the spatter capture plates. Dr. Aniruddha Das shared best practices for imaging particles with the optical microscope, which helped initiate this study. Dr. Vipin Tondare for measuring the sizes of the nickel superalloy 625 powder used during the experiment. Mr. Justin Whiting (DMG Mori) and Dr. Thien Phan (Lawrence Livermore National Laboratories) both inspired the capture plate method, and this work may not have existed without their experiments.

Appendix A. Traditional computer vision approaches for particle detection

In the main text, the images of the SCP were processed with a machine learning approach, but it is possible to use traditional computer vision (CV) approaches to identify particles in an image, which are otherwise called "blob detectors". The benefit of using blob detectors is that they are computationally simpler than machine learning approaches, thus making them quicker in operation. Blob detectors generally have two steps: first, they process the image with a filter to accentuate circular features, and second, they threshold the filtered image, segmenting it into pixels above and below the threshold. In the case of the current work, the pixels above the threshold would be spatter pixels, and the pixels below the threshold would be background pixels. The reader is referred to Ref. [66] for additional information on general blob detection and Ref. [67] for the use of traditional CV in detecting spatter in high-speed videos.

In this section, three techniques are tested: the Laplacian-of-Gaussian (LoG), Difference-of-Gaussians (DoG), and Determinant-of-Hessian (DoH) filters. The filters process the original image matrix, $\boldsymbol{I}$, as follows:

$$\boldsymbol{I}_{\boldsymbol{LoG}} = \sigma^2 \cdot \nabla^2 (\boldsymbol{G}_{\boldsymbol{\sigma}} * \boldsymbol{I}) \tag{A.1}$$

$$\boldsymbol{I}_{\boldsymbol{DoG}} = (\boldsymbol{G}_{\sigma_2} * \boldsymbol{I}) - (\boldsymbol{G}_{\sigma_1} * \boldsymbol{I}) \tag{A.2}$$

$$\boldsymbol{I}_{\boldsymbol{DoH}} = \frac{\partial^2}{\partial x^2}\boldsymbol{I} \cdot \frac{\partial^2}{\partial y^2}\boldsymbol{I} - \left(\frac{\partial^2}{\partial x \partial y}\boldsymbol{I}\right)^2 \tag{A.3}$$

where $\boldsymbol{I}_{\boldsymbol{LoG}}$, $\boldsymbol{I}_{\boldsymbol{DoG}}$, and $\boldsymbol{I}_{\boldsymbol{DoH}}$ are the image as processed by the LoG, DoG, and DoH filters, respectively; σ is the standard deviation of the gaussian filter, $\boldsymbol{G}_{\boldsymbol{\sigma}}$; ∇^2 is the Laplacian operator; and $*$ is the convolution operator. Coordinates x and y refer to the columns and rows of the image, respectively.

Each filter's parameters must be hand-tuned to achieve satisfactory performance: σ for LoG and σ_1 and σ_2 for DoG. DoH itself has no parameters, but it can benefit from having a gaussian filter applied to it before calculating the gradients, which also adds the parameter, σ. Each filter is typically discretized to apply convolution, and the size of this filter must be hand-tuned for each filter. Finally, the value used to threshold/segment the image is very important, and the optimal choice of this value changes according to the filter's other parameters.

Each of these filters is demonstrated in Fig. A.15, showing the image both after filtering and after thresholding the filtered image. Succinctly, the authors could not find a set of parameters for any of the above filters to achieve segmentation as good as the trained CNN, shown in Fig. A.15e. Each filter is clearly accentuating the particles in the image (seen in Fig. A.15b, c, and d), but they are also sensitive to the texture of the glue in the background. The glue's texture makes it difficult to then choose an appropriate threshold that cleanly segments spatter pixels from the glue.

The comparison in Fig. A.15 is not meant to imply that traditional methods cannot be used for the current task. Instead, it should be taken as evidence that the hand-tuning required by traditional methods presents a hurdle to properly extract the data within the images: spatter sizes, shapes, and landing sites. Due to this hurdle, the authors chose to devote time towards training a CNN to identify spatter rather than tuning a traditional computer vision method.

Appendix B. Segmentation model details

Fig. 3g showed the architecture of the segmentation model, a convolutional neural network (CNN). In the CNN, each convolution layer has a 3-by-3 kernel except for the output layer, which has a 1 by 1 kernel. Zero-padding is added at each convolution layer only to preserve the size of the image provided to it. Every convolution layer uses a stride and dilatation rate of 1. Max-pooling and up-sampling layers use 2-by-2 kernels with a stride of 2 to halve and double the image size, respectively.

The training dataset was also augmented for each epoch to assist in generalizability. At the start of each epoch, two additional copies of each patch were added to the training dataset and randomly augmented by one of the following operations: horizontal flip, vertical flip, random rotation up to 180°, random scaling from 50 % to 200 %, random brightness scale between 0.10 and 1.30, added gaussian noise up to 0.05, and jitter (random position shift) up to 60 pixels. For all augmentations except brightness scaling and gaussian noise, the corresponding pixel labels were transformed identically to their corresponding patch to maintain pixel-wise assignment. The original patches plus their two augmented copies then comprised the training dataset for that epoch, for which the model would predict the labels. Data augmentations expand the original dataset to make the model more reliable on unseen portions of the spatter capture plate.

Appendix C. Performance of CNN on blurry particles

The CNN was found to perform poorly on particles that appeared blurry in the microscope images. Some sections of the plate were slightly warped, meaning a small section was outside the focal plane of the microscope–this area was thus blurry and was segmented poorly by the CNN. Secondly, some agglomerates can be very tall and will result in a blurry image in some areas. Nonetheless, blurry particles appear to look more like the plate's background, which makes the CNN less reliable in these areas, as demonstrated in Fig. C.16.

Appendix D. Investigation of particles rebounding off the spatter capture plate

When particles hit the spatter capture plate (SCP), it is possible that they bounce, rebound, roll, or slide. To determine if this is the case, this section presents a brief series of high-magnification, high-speed videos, in which powder was sprayed on a bare plate with and without the glue used in the real experiment.

Fig. D.17 shows the imaging setup for this experiment. A Photron Nova S16 camera was used with an Infinity K2 Distamax Microscope using the model "STD" objective lens and four 2X-magnification NX tubes. A Veritas light emitting diode (LED) light was placed opposite the camera and aligned with its field of view. The plate/surface-of-interest was then placed in focus between the light and the camera to achieve a high-contrast video of the powder. Several videos were recorded at 10 kHz frame rate. The exposure time of the camera was adjusted to avoid overexposure of the images.

For videos which observed landing on the glue-coated SCP, the glue was applied about five minutes before blowing any powder across it—a time frame similar to that of the experiment in the main text. Powder was blown parallel to the plate using a rubber "puffer". It should be noted that the amount of powder blown over the plate is expected to be much more than the amount of spatter produced in printing, making this experiment potentially more chaotic than what would transpire in the real experiment. These trials should be considered the worst-case scenario.

Video 1 first shows the behavior of powder over the SCP without glue. This video shows how powder chaotically travel across the plate, rebounding with itself and overall not being captured by the plate. There is significant upwards movement in the powder, with some

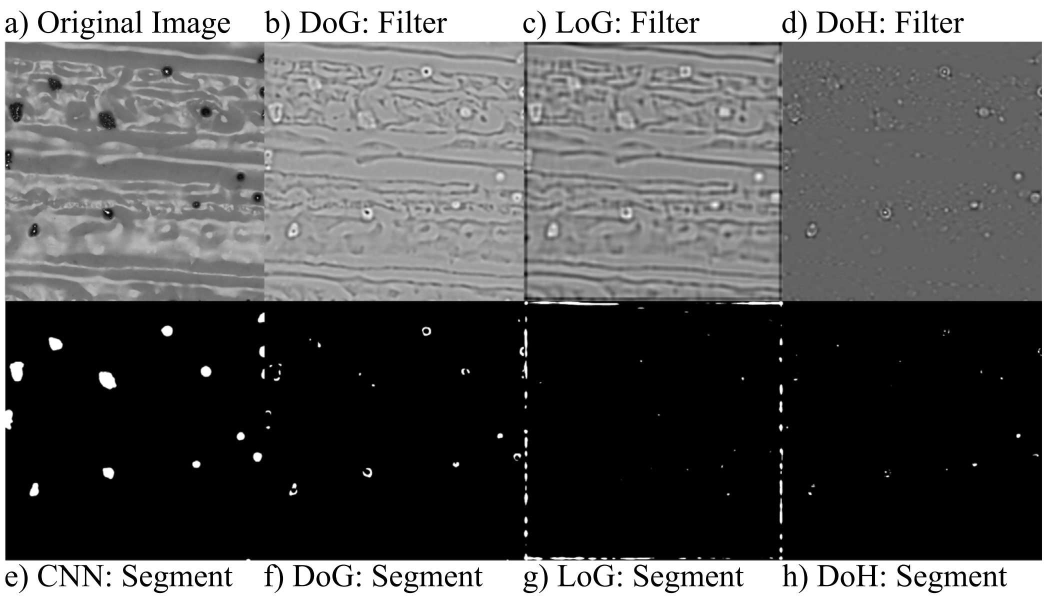

Fig. A.15. Comparison of traditional CV filters in identifying spatter particles in an image. Each filter was hand-tuned to achieve the best possible performance.

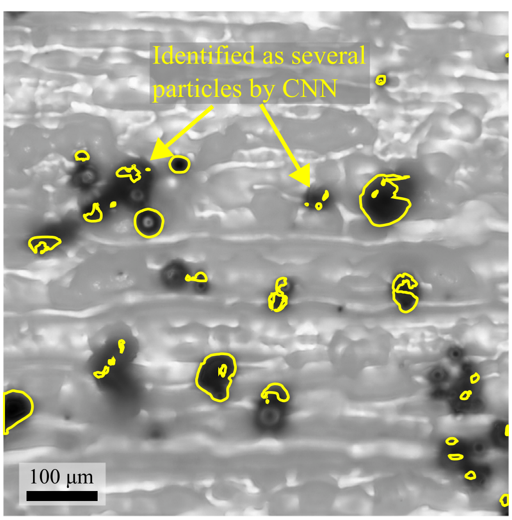

Fig. C.16. Example of CNN performance on blurry areas, which were excluded from analysis of landing sites and sizes.

powder particles bouncing as high as 4 mm above the plate and being carried away by the flow above the plate.

Video 2, the video of powder landing on the SCP with glue, shows the opposite behavior. Particles travel down towards the plate, stopping immediately upon landing. The particles travel at similar speeds to those seen in Video 1, so the forces of particle impact on the plate should be similar between these two videos. Curiously, there is less powder in the background above the plate in Video 2 compared to Video 1. This difference is attributed to (1) the variability of powder ejected by the puffer and (2) the possibility that some powder particles landed on the glue outside of the camera's field-of-view, presenting less powder to land on the plate further downstream.

Extrapolating from Videos 1 and 2, it is largely expected that the spatter landing sites observed in the SCP are where they would have landed without the SCP. Particles landing on the glue coated plate do not rebound, which is similar to the behavior expected when the particle hits the powder bed. While this experiment only tested particles up to about 63 μm, it is also expected that larger particles and agglomerates would have similarly been captured by the glue, given their larger surface area to contact the glue. This experiment was also repeated for other surfaces and powder materials for the benefit of future works, the results of which are summarized in Table D.3.

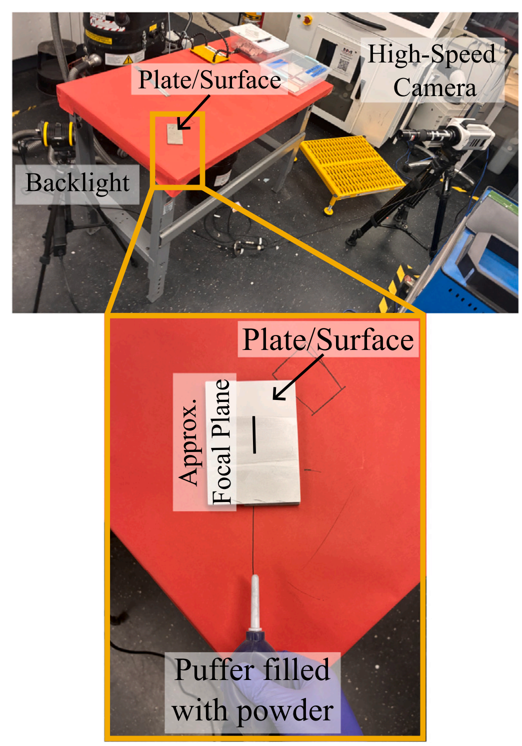

Fig. D.17. Pictures of the experiment to investigate powder's landing behavior.

Table D.3
Summary of powder impact behavior for various surfaces.

Powder material[a]	Surface type	Description of impact behavior
AlSi10Mg	Bare metal	Rolling, sliding, high rebounds
	Copper SEM[b] tape	Sticks upon landing
	SCP without glue	Less rebounding than bare metal with rolling and sliding
WC 17Ni[c]	Bare metal	Multiple rebounds for all particles, plus sliding and rolling
	Copper SEM tape	Sticks upon landing
	SCP with glue	Sticks upon landing, rebounds observed but are rare and smaller than bare metal[d]
Nickel superalloy 625	Bare metal	Rebounding, sliding, and rolling
	Copper SEM tape	Sticks upon landing
	Carbon SEM tape	Sticks upon landing
	SCP without glue	Many rebounds with sliding and rolling
	SCP with glue	Sticks upon landing, rebounds observed but rare and smaller than bare metal[d]

[a] All powders had similar size ranges, with a D10 and D90 of about 20 μm and 60 μm, respectively, according to the manufacturers.
[b] SEM - Scanning Electron Microscope.
[c] WC 17Ni is a tungsten carbide powder with nickel binder particles.
[d] Some particles rebounded after the plate filled up due to collisions with captured particles. See Video 3.

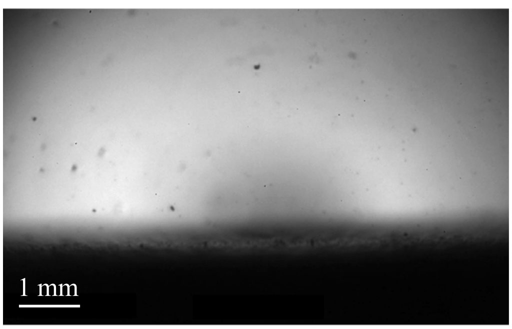

Video 1. Powder landing on SCP **without glue**. (Please see supplemental file `Inc625_PaintedPlateNOGLUE.mp4` to watch the video.)

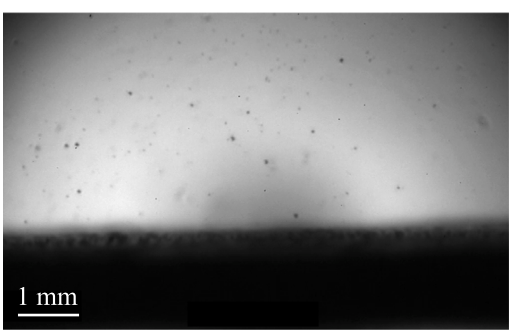

Video 2. Powder landing on spatter capture plate **with glue**. (Please see supplemental file `Inc625_PaintedPlateGlue.mp4` to watch the video.)

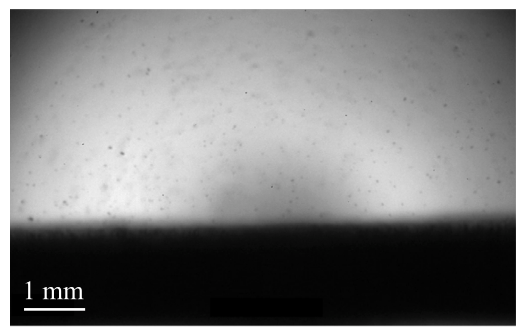

Video 3. Powder landing on spatter capture plate **with glue**, three seconds after the end of Video 2, when the plate began to fill up. (Please see supplemental file `Inc625_PaintedPlateGlue_Filled.mp4` to watch the video.)

While spatter particles are generally expected to be captured by the SCP, these experiments did show a potential rare source of error, shown in Video 3. In this video, particles have landed on the glue-coated SCP for about three seconds since the end of Video 2, filling the plate and leaving less surface area for glue to capture a particle. This video shows two particles that rebound off of a previously-captured particle, causing that particle to land somewhere else. This situation is unlikely in the current work, given that the SCP was used only for one layer and that the SCP was not entirely filled even in the highest spatter-density regions, as shown in Fig. D.18a. Future uses of the SCP method should be aware of this limitation, for the more particles landing on the plate, the higher likelihood of a random collision somewhere on the plate.

One more phenomena that this experiment does not account for is the potentially high temperatures of spatter particles. Some of the hottest spatter particles, in theory, could be hot enough to degrade the adhesive used on the SCP, which could adversely affect the sticking behavior observed in these high-speed videos. To investigate this potential effect, the pictures of the SCP in Fig. D.18 can be observed.

Fig. D.18 shows a microscope image from the SCP immediately downstream from the printed part. At a low magnification (D.18a), the glue's texture and color look uniform, despite the scattered spatter particles across the image. Fig. D.18b then zooms into an area closer to the part, where Fig. D.18c and d focus on two large spatter particles with diameters close to 100 μm. Being much larger than the powder itself and having slightly nonspherical shapes, these two particles were undoubtedly melted sometime during their ejections. Furthermore, given that their landing sites were very close to the part (within 13 mm from the bottom edge), these particles would have very likely been molten/hot upon landing. Despite these likely high temperatures, the glue surrounding and underneath the particle is not so different from the glue seen elsewhere on the plate. There are also no other witness marks near these particles that indicate sliding or bouncing from a previous interaction with the plate.

While there seems to be no adverse interaction between hot spatter particles and the glue, future works which use spatter capture plates with a higher melting-temperature alloy (e.g., tungsten alloys) could

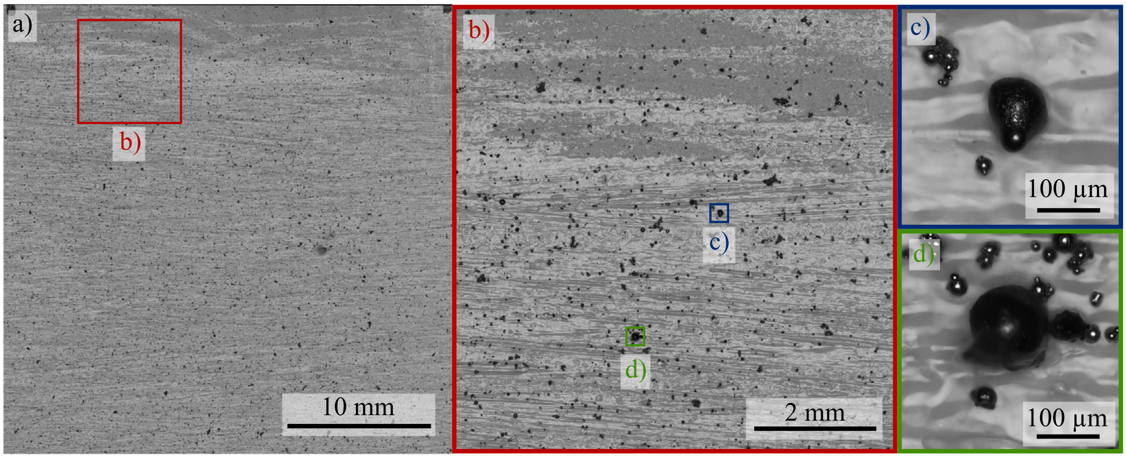

Fig. D.18. Images from Spatter Capture Plate immediately downstream from the printed part. Region (b) ranges from 4 mm to 13 mm downstream from the edge of the printed part. The two black marks in the upper-left and upper-right corners of subfigure a are the fiducial marks indicating the edges of the part.

encounter such a phenomena, and they may want to take care in using a long-tack adhesive that is suitable for such temperatures.

Appendix E. Supplementary data

Supplementary material related to this article can be found online at https://doi.org/10.1016/j.addma.2026.105303.

Data availability

Data from this work is hosted on data.nist.gov under the following DOI: https://doi.org/10.18434/mds2-4277.

References

[1] S. Chowdhury, N. Yadaiah, C. Prakash, S. Ramakrishna, S. Dixit, L.R. Gulta, D. Buddhi, Laser powder bed fusion: A state-of-the-art review of the technology, materials, properties & defects, and numerical modelling, J. Mater. Res. Technol. (2022) S2238785422011607, http://dx.doi.org/10.1016/j.jmrt.2022.07.121, URL https://linkinghub.elsevier.com/retrieve/pii/S2238785422011607.

[2] T. Ohtsuki, L. Smith, M. Tang, P.C. Pistorius, Origin of oxides and oxide-related pores in laser powder bed fusion parts, in: N. Shamsaei, M. Seifi (Eds.), Structural Integrity of Additive Manufactured Materials & Parts, ASTM International, 100 Barr Harbor Drive, PO Box C700, West Conshohocken, PA 19428-2959, 2020, pp. 45–60, http://dx.doi.org/10.1520/STP163120190137, URL https://www.astm.org/doiLink.cgi?STP163120190137.

[3] N. Bonato, F. Zanini, S. Carmignato, Prediction of spatter-related defects in metal laser powder bed fusion by analytical and machine learning modelling applied to off-axis long-exposure monitoring, Addit. Manuf. 94 (2024) 104504, http://dx.doi.org/10.1016/j.addma.2024.104504, URL https://linkinghub.elsevier.com/retrieve/pii/S2214860424005505.

[4] M. Laleh, A.E. Hughes, S. Yang, J. Wang, J. Li, A.M. Glenn, W. Xu, M.Y. Tan, A critical insight into lack-of-fusion pore structures in additively manufactured stainless steel, Addit. Manuf. 38 (2021) 101762, http://dx.doi.org/10.1016/j.addma.2020.101762, URL https://linkinghub.elsevier.com/retrieve/pii/S2214860420311349.

[5] C. Schwerz, A. Raza, X. Lei, L. Nyborg, E. Hryha, H. Wirdelius, In-situ detection of redeposited spatter and its influence on the formation of internal flaws in laser powder bed fusion, Addit. Manuf. 47 (2021) 102370, http://dx.doi.org/10.1016/j.addma.2021.102370, URL https://linkinghub.elsevier.com/retrieve/pii/S2214860421005248.

[6] Z. Snow, L. Scime, A. Ziabari, B. Fisher, V. Paquit, Observation of spatter-induced stochastic lack-of-fusion in laser powder bed fusion using in situ process monitoring, Addit. Manuf. 61 (2023) 103298, http://dx.doi.org/10.1016/j.addma.2022.103298, URL https://linkinghub.elsevier.com/retrieve/pii/S221486042200687X.

[7] D. Wang, S. Wu, F. Fu, S. Mai, Y. Yang, Y. Liu, C. Song, Mechanisms and characteristics of spatter generation in SLM processing and its effect on the properties, Mater. Des. 117 (2017) 121–130, http://dx.doi.org/10.1016/j.matdes.2016.12.060, URL https://linkinghub.elsevier.com/retrieve/pii/S0264127516315866.

[8] T.M. Wischeropp, C. Emmelmann, M. Brandt, A. Pateras, Measurement of actual powder layer height and packing density in a single layer in selective laser melting, Addit. Manuf. 28 (2019) 176–183, http://dx.doi.org/10.1016/j.addma.2019.04.019, URL https://linkinghub.elsevier.com/retrieve/pii/S2214860418306444.

[9] N. Bonato, F. Zanini, S. Carmignato, Enhanced tomographic porosity measurements in laser powder bed fusion metal parts using a novel reference object, J. Manuf. Process. 155 (2025) 1049–1061, http://dx.doi.org/10.1016/j.jmapro.2025.10.076, URL https://linkinghub.elsevier.com/retrieve/pii/S1526612525011685.

[10] Z. Snow, C. Cummings, E.W. Reutzel, A. Nassar, K. Abbot, P. Guerrier, S. Kelly, S. McKown, J. Blecher, R. Overdorff, Analysis of factors affecting fatigue performance of HIP'd laser-based powder bed fusion Ti–6Al–4V coupons, Mater. Sci. Eng.: A 864 (2023) 144575, http://dx.doi.org/10.1016/j.msea.2022.144575, URL https://linkinghub.elsevier.com/retrieve/pii/S0921509322019554.

[11] V.B. Vukkum, T. Sanborn, J. Shepherd, S. Saptarshi, R. Basu, T. Horn, R.K. Gupta, Influence of spatter on porosity, microstructure, and corrosion of additively manufactured stainless steel printed using different island size, Crystals 14 (4) (2024) 328, http://dx.doi.org/10.3390/cryst14040328, URL https://www.mdpi.com/2073-4352/14/4/328.

[12] C. Kantzos, J. Pauza, R. Cunningham, S.P. Narra, J. Beuth, A. Rollett, An investigation of process parameter modifications on additively manufactured Inconel 718 parts, J. Mater. Eng. Perform. 28 (2) (2019) 620–626, http://dx.doi.org/10.1007/s11665-018-3612-3, URL http://link.springer.com/10.1007/s11665-018-3612-3.

[13] A.N.D. Gasper, B. Szost, X. Wang, D. Johns, S. Sharma, A.T. Clare, I.A. Ashcroft, Spatter and oxide formation in laser powder bed fusion of Inconel 718, Addit. Manuf. 24 (2018) 446–456, http://dx.doi.org/10.1016/j.addma.2018.09.032, URL https://linkinghub.elsevier.com/retrieve/pii/S2214860418304524.

[14] R. Esmaeilizadeh, U. Ali, A. Keshavarzkermani, Y. Mahmoodkhani, E. Marzbanrad, E. Toyserkani, On the effect of spatter particles distribution on the quality of Hastelloy X parts made by laser powder-bed fusion additive manufacturing, J. Manuf. Process. 37 (2019) 11–20, http://dx.doi.org/10.1016/j.jmapro.2018.11.012, URL https://linkinghub.elsevier.com/retrieve/pii/S1526612518303979.

[15] H. Zhang, C.K.P. Vallabh, X. Zhao, Influence of spattering on in-process layer surface roughness during laser powder bed fusion, J. Manuf. Process. 104 (2023) 289–306, http://dx.doi.org/10.1016/j.jmapro.2023.08.058, URL https://linkinghub.elsevier.com/retrieve/pii/S1526612523008484.

[16] S.J.A. Hocker, A.R. Kitahara, B. Richter, S.-H. Chu, B. Widener, P.W. Spaeth, J.N. Zalameda, E.H. Glaessgen, A novel additive manufacturing process metric for predicting spatter-related porosity in laser powder bed fusion, Integr. Mater. Manuf. Innov. (2024) http://dx.doi.org/10.1007/s40192-024-00376-0, URL https://link.springer.com/10.1007/s40192-024-00376-0.

[17] A. Mostafaei, C. Zhao, Y. He, S. Reza Ghiaasiaan, B. Shi, S. Shao, N. Shamsaei, Z. Wu, N. Kouraytem, T. Sun, J. Pauza, J.V. Gordon, B. Webler, N.D. Parab, M. Asherloo, Q. Guo, L. Chen, A.D. Rollett, Defects and anomalies in powder bed fusion metal additive manufacturing, Curr. Opin. Solid State Mater. Sci. 26 (2) (2022) 100974, http://dx.doi.org/10.1016/j.cossms.2021.100974, URL https://linkinghub.elsevier.com/retrieve/pii/S1359028621000772.

[18] T. Reddy, A. Ngo, J.P. Miner, C. Gobert, J.L. Beuth, A.D. Rollett, J.J. Lewandowski, S.P. Narra, Fatigue-based process window for laser beam powder bed fusion additive manufacturing, Int. J. Fatigue 187 (2024) 108428, http://dx.doi.org/10.1016/j.ijfatigue.2024.108428, URL https://linkinghub.elsevier.com/retrieve/pii/S014211232400286X.

[19] A.T. Sutton, C.S. Kriewall, M.C. Leu, J.W. Newkirk, B. Brown, Characterization of laser spatter and condensate generated during the selective laser melting of 304L stainless steel powder, Addit. Manuf. 31 (2020) 100904, http://dx.doi.org/10.1016/j.addma.2019.100904, URL https://linkinghub.elsevier.com/retrieve/pii/S2214860419302787.

[20] M. Simonelli, C. Tuck, N.T. Aboulkhair, I. Maskery, I. Ashcroft, R.D. Wildman, R. Hague, A study on the laser spatter and the oxidation reactions during selective laser melting of 316L stainless steel, Al-Si10-Mg, and Ti-6Al-4V, Metall. Mater. Trans. A 46 (9) (2015) 3842–3851, http://dx.doi.org/10.1007/s11661-015-2882-8, URL http://link.springer.com/10.1007/s11661-015-2882-8.

[21] T. Fedina, J. Sundqvist, A.F.H. Kaplan, Spattering and oxidation phenomena during recycling of low alloy steel powder in Laser Powder Bed Fusion, Mater. Today Commun. 27 (2021) 102241, http://dx.doi.org/10.1016/j.mtcomm.2021.102241, URL https://linkinghub.elsevier.com/retrieve/pii/S2352492821002336.

[22] J. Yin, D. Wang, H. Wei, L. Yang, L. Ke, M. Hu, W. Xiong, G. Wang, H. Zhu, X. Zeng, Dual-beam laser-matter interaction at overlap region during multi-laser powder bed fusion manufacturing, Addit. Manuf. 46 (2021) 102178, http://dx.doi.org/10.1016/j.addma.2021.102178, https://www.sciencedirect.com/science/article/pii/S2214860421003419.

[23] B. Abranovic, Machine Learning-Enabled Process Monitoring and Process Development Across Additive Platforms (Ph.D. thesis), Carnegie Mellon University, 2022, ISBN: 9798379437824 Publication Title: ProQuest Dissertations and Theses. URL https://www.proquest.com/dissertations-theses/machine-learning-enabled-process-monitoring/docview/2806654940/se-2.

[24] A.B. Anwar, Q.-C. Pham, Study of the spatter distribution on the powder bed during selective laser melting, Addit. Manuf. 22 (2018) 86–97, http://dx.doi.org/10.1016/j.addma.2018.04.036, URL https://linkinghub.elsevier.com/retrieve/pii/S2214860418300897.

[25] G. Repossini, V. Laguzza, M. Grasso, B.M. Colosimo, On the use of spatter signature for in-situ monitoring of Laser Powder Bed Fusion, Addit. Manuf. 16 (2017) 35–48, http://dx.doi.org/10.1016/j.addma.2017.05.004, 00000. URL http://www.sciencedirect.com/science/article/pii/S2214860416303402.

[26] J. Berez, C. Saldaña, On the nature and causes of spatter redistribution in laser powder bed fusion, J. Manuf. Process. 127 (2024) 531–544, http://dx.doi.org/10.1016/j.jmapro.2024.07.143, Publisher: Elsevier BV. URL https://linkinghub.elsevier.com/retrieve/pii/S1526612524008065.

[27] S.Z. Uddin, Laser Powder Bed Fusion and in Situ Process Monitoring of Tall Thin-Walled Structures (Ph.D. thesis), Carnegie Mellon University, 2022, ISBN: 9798352694060 Publication Title: ProQuest Dissertations and Theses. URL https://www.proquest.com/dissertations-theses/laser-powder-bed-fusion-situ-process-monitoring/docview/2720949048/se-2.

[28] N. O'Brien, S.Z. Uddin, J. Weaver, J. Jones, S. Singh, J. Beuth, Computational analysis and experiments of spatter transport in a laser powder bed fusion machine, Addit. Manuf. 84 (2024) 104133, http://dx.doi.org/10.1016/j.addma.2024.104133, URL https://linkinghub.elsevier.com/retrieve/pii/S2214860424001799.

[29] T.-T. Ikeshoji, M. Yonehara, C. Kato, Y. Yanaga, K. Takeshita, H. Kyogoku, Spattering mechanism of laser powder bed fusion additive manufacturing on heterogeneous surfaces, Sci. Rep. 12 (1) (2022) 20384, http://dx.doi.org/10.1038/s41598-022-24828-9, URL https://www.nature.com/articles/s41598-022-24828-9.

[30] D. Brummerloh, D. Jutkuhn, Z. Yang, A. Penn, C. Emmelmann, Stereo camera based in-situ monitoring of L-PBF process stability by spatter detection, Adv. Precis. Addit. Manuf. (2021).

[31] S. Ly, A.M. Rubenchik, S.A. Khairallah, G. Guss, M.J. Matthews, Metal vapor micro-jet controls material redistribution in laser powder bed fusion additive manufacturing, Sci. Rep. 7 (1) (2017) 4085, http://dx.doi.org/10.1038/s41598-017-04237-z, URL http://www.nature.com/articles/s41598-017-04237-z.

[32] A.B. Anwar, I.H. Ibrahim, Q.-C. Pham, Spatter transport by inert gas flow in selective laser melting: A simulation study, Powder Technol. 352 (2019) 103–116, http://dx.doi.org/10.1016/j.powtec.2019.04.044, URL https://linkinghub.elsevier.com/retrieve/pii/S003259101930292X.

[33] M. Lutter-Günther, M. Bröker, T. Mayer, S. Lizak, C. Seidel, G. Reinhart, Spatter formation during laser beam melting of AlSi10Mg and effects on powder quality, Procedia CIRP 74 (2018) 33–38, http://dx.doi.org/10.1016/j.procir.2018.08.008, URL https://linkinghub.elsevier.com/retrieve/pii/S2212827118307911.

[34] J.A. Slotwinski, E.J. Garboczi, P.E. Stutzman, C.F. Ferraris, S.S. Watson, M.A. Peltz, Characterization of metal powders used for additive manufacturing, J. Res. Natl. Inst. Stand. Technol. 119 (2014) 460, http://dx.doi.org/10.6028/jres.119.018, URL https://nvlpubs.nist.gov/nistpubs/jres/119/jres.119.018.pdf.

[35] X. Zhang, B. Cheng, C. Tuffile, Simulation study of the spatter removal process and optimization design of gas flow system in laser powder bed fusion, Addit. Manuf. 32 (2020) 101049, http://dx.doi.org/10.1016/j.addma.2020.101049, URL https://linkinghub.elsevier.com/retrieve/pii/S2214860419317749.

[36] J. Altmeppen, R. Nekic, P. Wagenblast, S. Staudacher, Transient simulation of particle transport and deposition in the laser powder bed fusion process: A new approach to model particle and heat ejection from the melt pool, Addit. Manuf. 46 (2021) 102135, http://dx.doi.org/10.1016/j.addma.2021.102135, URL https://linkinghub.elsevier.com/retrieve/pii/S2214860421002992.

[37] J.S. Weaver, A. Schlenoff, D.C. Deisenroth, S.P. Moylan, Inert Gas Flow Speed Measurements in Laser Powder Bed Fusion Additive Manufacturing, Tech. rep., National Institute of Standards and Technology, 2021, http://dx.doi.org/10.6028/NIST.AMS.100-43, URL https://nvlpubs.nist.gov/nistpubs/ams/NIST.AMS.100-43.pdf.

[38] J. Berez, E. Dushaj, J. Weaver, D. Deisenroth, S. Moylan, C. Saldaña, Development and Validation of a focus offset measurement method for laser powder bed fusion machines, 2026, In-Draft.

[39] M.J. Matthews, G. Guss, S.A. Khairallah, A.M. Rubenchik, P.J. Depond, W.E. King, Denudation of metal powder layers in laser powder bed fusion processes, Acta Mater. 114 (2016) 33–42, http://dx.doi.org/10.1016/j.actamat.2016.05.017, URL https://linkinghub.elsevier.com/retrieve/pii/S135964541630355X.

[40] O. Ronneberger, P. Fischer, T. Brox, U-Net: Convolutional networks for biomedical image segmentation, in: N. Navab, J. Hornegger, W.M. Wells, A.F. Frangi (Eds.), Medical Image Computing and Computer-Assisted Intervention – MICCAI 2015, in: Lecture Notes in Computer Science, vol. 9351, Springer International Publishing, Cham, 2015, pp. 234–241, http://dx.doi.org/10.1007/978-3-319-24574-4_28, URL http://link.springer.com/10.1007/978-3-319-24574-4_28.

[41] Dragonfly 2024.1, 2024, URL https://dragonfly.comet.tech/.

[42] M.D. Zeiler, ADADELTA: An adaptive learning rate method, 2012, http://dx.doi.org/10.48550/ARXIV.1212.5701, Version Number: 1. URL https://arxiv.org/abs/1212.5701.

[43] G. Bradski, The OpenCV library, Dr. Dobb's J. Softw. Tools (2000).

[44] J.W. Pratt, J.D. Gibbons, Kolmogorov-Smirnov two-sample tests, in: Concepts of Nonparametric Theory, in: Springer Series in Statistics, Springer New York, New York, NY, 1981, pp. 318–344, http://dx.doi.org/10.1007/978-1-4612-5931-2_7, URL http://link.springer.com/10.1007/978-1-4612-5931-2_7.

[45] J.P. Miner, A. Ngo, C. Gobert, T. Reddy, J.J. Lewandowski, A.D. Rollett, J. Beuth, S.P. Narra, Impact of melt pool geometry variability on lack-of-fusion porosity and fatigue life in powder bed fusion-laser beam Ti–6Al–4V, Addit. Manuf. 95 (2024) 104506, http://dx.doi.org/10.1016/j.addma.2024.104506, Publisher: Elsevier BV. URL https://linkinghub.elsevier.com/retrieve/pii/S2214860424005529.

[46] S. Raschka, Model evaluation, model selection, and algorithm selection in machine learning, 2020, arXiv:1811.12808 [cs, stat]. URL http://arxiv.org/abs/1811.12808.

[47] Z.A. Young, Q. Guo, N.D. Parab, C. Zhao, M. Qu, L.I. Escano, K. Fezzaa, W. Everhart, T. Sun, L. Chen, Types of spatter and their features and formation mechanisms in laser powder bed fusion additive manufacturing process, Addit. Manuf. 36 (2020) 101438, http://dx.doi.org/10.1016/j.addma.2020.101438, URL https://linkinghub.elsevier.com/retrieve/pii/S2214860420308101.

[48] A.R. Nassar, M.A. Gundermann, E.W. Reutzel, P. Guerrier, M.H. Krane, M.J. Weldon, Formation processes for large ejecta and interactions with melt pool formation in powder bed fusion additive manufacturing, Sci. Rep. 9 (1) (2019) 5038, http://dx.doi.org/10.1038/s41598-019-41415-7, URL https://www.nature.com/articles/s41598-019-41415-7.

[49] J.S. Weaver, A. Schlenoff, D. Deisenroth, S.P. Moylan, Hot-wire anemometer gas speed measurements in a commercial laser powder bed fusion machine, 2022, http://dx.doi.org/10.18434/MDS2-2857, Artwork Size: 6 files, 11.3 MB Medium: application/pdf, application/x-zip-compressed, text/csv, text/plain Pages: 6 files, 11.3 MB. URL https://data.nist.gov/od/id/mds2-2857.

[50] T.M. Inc, MATLAB version: 24.2.0 (R2024b), 2024, URL https://www.mathworks.com.

[51] ANSYS, ANSYS Fluent User Guide, ANSYS Inc., 2021.

[52] B.E. Poling, J.M. Prausnitz, J.P. O'Connell, The Properties of Gases and Liquids, fifth ed., in: McGraw-Hill International Editions Chemical Engineering Series, McGraw-Hill, New York, NY, 2001.

[53] S. Chen, P. Chen, J. Fu, Drag and lift forces acting on linear and irregular agglomerates formed by spherical particles, Phys. Fluids 34 (2) (2022) 023307, http://dx.doi.org/10.1063/5.0082653, URL https://pubs.aip.org/pof/article/34/2/023307/2846827/Drag-and-lift-forces-acting-on-linear-and.

[54] R. Rorato, M. Arroyo, E. Andò, A. Gens, Sphericity measures of sand grains, Eng. Geol. 254 (2019) 43–53, http://dx.doi.org/10.1016/j.enggeo.2019.04.006, URL https://linkinghub.elsevier.com/retrieve/pii/S0013795218317800.

[55] J.R. Grace, A. Ebneyamini, Connecting particle sphericity and circularity, Particuology 54 (2021) 1–4, http://dx.doi.org/10.1016/j.partic.2020.09.006, URL https://linkinghub.elsevier.com/retrieve/pii/S1674200120300936.

[56] C.R.I. Clayton, C.O.R. Abbireddy, R. Schiebel, A method of estimating the form of coarse particulates, Géotechnique 59 (6) (2009) 493–501, http://dx.doi.org/10.1680/geot.2007.00195, URL http://www.emerald.com/jgeot/article/59/6/493-501/402402.

[57] F. Podczeck, J.M. Newton, The evaluation of a three-dimensional shape factor for the quantitative assessment of the sphericity and surface roughness of pellets, Int. J. Pharm. 124 (2) (1995) 253–259, http://dx.doi.org/10.1016/0378-5173(95)00096-2, URL https://linkinghub.elsevier.com/retrieve/pii/0378517395000962.

[58] J.M. Rodriguez, T. Edeskär, S. Knutsson, Particle shape quantities and measurement techniques–A review, Electron. J. Geotech. Eng. 18/A (2013) 169–198, URL https://www.diva-portal.org/smash/record.jsf?pid=diva2%3A976352&dswid=7346.

[59] S.A. Morsi, A.J. Alexander, An investigation of particle trajectories in two-phase flow systems, J. Fluid Mech. 55 (02) (1972) 193, http://dx.doi.org/10.1017/S0022112072001806, URL http://www.journals.cambridge.org/abstract_S0022112072001806.

[60] R. Barati, S.A.A.S. Neyshabouri, G. Ahmadi, Development of empirical models with high accuracy for estimation of drag coefficient of flow around a smooth sphere: An evolutionary approach, Powder Technol. 257 (2014) 11–19, http://dx.doi.org/10.1016/j.powtec.2014.02.045, URL https://linkinghub.elsevier.com/retrieve/pii/S003259101400182X.

[61] P. Bidare, I. Bitharas, R.M. Ward, M.M. Attallah, A.J. Moore, Fluid and particle dynamics in laser powder bed fusion, Acta Mater. 142 (2018) 107–120, http://dx.doi.org/10.1016/j.actamat.2017.09.051, URL https://linkinghub.elsevier.com/retrieve/pii/S1359645417308170.

[62] X. Li, C. Zhao, T. Sun, W. Tan, Revealing transient powder-gas interaction in laser powder bed fusion process through multi-physics modeling and high-speed synchrotron x-ray imaging, Addit. Manuf. 35 (2020) 101362, http://dx.doi.org/10.1016/j.addma.2020.101362, URL https://linkinghub.elsevier.com/retrieve/pii/S221486042030734X.

[63] A. Masmoudi, R. Bolot, C. Coddet, Investigation of the laser–powder–atmosphere interaction zone during the selective laser melting process, J. Mater. Process. Technol. 225 (2015) 122–132, http://dx.doi.org/10.1016/j.jmatprotec.2015.05.008, URL https://linkinghub.elsevier.com/retrieve/pii/S0924013615002083.

[64] A. Hölzer, M. Sommerfeld, Lattice Boltzmann simulations to determine drag, lift and torque acting on non-spherical particles, Comput. & Fluids 38 (3) (2009) 572–589, http://dx.doi.org/10.1016/j.compfluid.2008.06.001, URL https://linkinghub.elsevier.com/retrieve/pii/S0045793008001175.

[65] C.T. Crowe, J.D. Schwarzkopf, M. Sommerfeld, Y. Tsuji, Multiphase Flows with Droplets and Particles, CRC Press, 2011, http://dx.doi.org/10.1201/b11103, https://www.taylorfrancis.com/books/9781439840511.

[66] M. Moukthika, Blob detection using OpenCV, 2025, URL https://opencv.org/blob-detection-using-opencv/#h-what-is-a-blob.

[67] E. Eschner, T. Staudt, M. Schmidt, 3D particle tracking velocimetry for the determination of temporally resolved particle trajectories within laser powder bed fusion of metals, Int. J. Extrem. Manuf. 1 (3) (2019) 035002, http://dx.doi.org/10.1088/2631-7990/ab3de9, URL https://iopscience.iop.org/article/10.1088/2631-7990/ab3de9.